Research article

Two episodes of Mesozoic mafic magmatism in the Nansha Block: Tectonic transition from continental arc to back-arc basin

Xiu-Quan Miao [a,b,c,d], Xiao-Long Huang [a,b,c,*], Wen Yan [c,e], Fan Yang [a,b,c], Wan-Feng Zhang [a,b,c], Yang Yu [a,b,c], Yu-Xin Cai [a,b,c,d], Sheng-Zhu Zhu [a,b,c,d]

[a] State Key Laboratory of Isotope Geochemistry, Guangzhou Institute of Geochemistry, Chinese Academy of Sciences, Guangzhou 510640, China
[b] CAS Center for Excellence in Deep Earth Science, Guangzhou 510640, China
[c] Southern Marine Science and Engineering Guangdong Laboratory (Guangzhou), Guangzhou 511458, China
[d] University of Chinese Academy of Sciences, Beijing 100049, China
[e] CAS Key Laboratory of Ocean and Marginal Sea Geology, South China Sea Institute of Oceanology, Innovation Academy of South China Sea Ecology and Environmental Engineering, Chinese Academy of Sciences, Guangzhou 510301, China

ARTICLE INFO

ABSTRACT

It has been proposed that the proto-South China Sea (PSCS) existed in the southeastern continental margin of the South China Block (SCB) before the opening of the present South China Sea (SCS). However, the age of initial spreading and the geodynamics of the opening of the PSCS remain enigmatic. Here we present geochronological and geochemical data for diorite and diabase samples from Well NK-1, which was drilled into the Nansha Block in the Dangerous Grounds area of the southern SCS, to investigate their petrogenesis and their association with the formation of the PSCS. The Early Jurassic diorites (ca. 177 Ma) are geochemically similar to continental arc basalt, with enrichment in Rb, Ba, Pb, and Sr, and pronounced negative Nb, Ta, and Ti anomalies. They were originated from a mantle source metasomatized by subducted-sediment-derived melts in a continental arc setting related to subduction of the Paleo-Pacific plate beneath the SCB. The Early Cretaceous diabases (ca. 124 Ma) are compositionally similar to back-arc basin basalt, with enrichment in Rb, Ba, and Pb, and negligible Nb, Ta, Ti, Zr, and Hf anomalies. The mantle source of the diabases was metasomatized by aqueous fluids derived from the subducted slab in a back-arc basin associated with subduction of the Paleo-Pacific plate. Furthermore, the diabase samples are geochemically similar to mafic rocks and ophiolite complexes previously regarded as remnants of the PSCS oceanic crust. Therefore, the Early Cretaceous diabases in the Nansha Block are interpreted as representing coeval magmatism of the nascent ocean of the PSCS, indicating that the PSCS during the Early Cretaceous was a spreading back-arc basin associated with retreat of the subducting Paleo-Pacific plate.

1. Introduction

The South China Sea (SCS) is the largest marginal sea of the western Pacific Ocean. Several models have been proposed for the initial formation and evolution of the SCS, including tectonic extrusion along the Red River fault due to India–Eurasia collision (Briais et al., 1993; Tapponnier et al., 1982), back-arc extension due to subduction of the Neo-Tethyan oceanic plate between the Australian and Eurasian plates (Sun, 2016), and slab pull owing to subduction of the proto-SCS (PSCS; Taylor and Hayes, 1982; Wu and Suppe, 2018). The slab pull model proposes that the PSCS was a Mesozoic oceanic basin that formed before the opening of the SCS but was subsequently subducted beneath the Borneo–Sabah Block (Taylor and Hayes, 1982; Wu and Suppe, 2018). Slab-shaped swaths of detached, subhorizontal tomographic anomalies beneath the SCS and Borneo Block at depths of 450–700 and 800–900 km have been interpreted as the previously subducted northern and southern PSCS slabs, respectively. Subduction of the PSCS oceanic lithosphere beneath the Borneo Block is further supported by the presence of Late Cretaceous–early Eocene ophiolites in the northern Borneo Block (e.g., Hall et al., 2008) and a much thicker crust (~39.1 km) in the Sabah area of NE Borneo related to subduction–accretion (Gao et al., 2020). Owing to complete subduction of the PSCS lithosphere, the initial

---

* Corresponding author at: State Key Laboratory of Isotope Geochemistry, Guangzhou Institute of Geochemistry, Chinese Academy of Sciences, Guangzhou 510640, China.
  E-mail address: xlhuang@gig.ac.cn (X.-L. Huang).

spreading age and geodynamic mechanism of the opening of the PSCS remain enigmatic. The PSCS has been interpreted variously as a bay in the Paleo-Pacific Ocean during the Middle Triassic, part of the Meso-Tethys Ocean, or a back-arc basin formed by subduction of the Paleo-Pacific or Neo-Tethyan plate during the Cretaceous (Morley, 2012; Sun, 2016). Therefore, constraining the age of opening and tectonic

attributes of the PSCS is a key requirement for understanding the tectonic evolution of Southeast Asia, as the formation of the PSCS was a consequence of Mesozoic–Cenozoic plate interactions among the South China Block (SCB), Paleo-Pacific plate, and Borneo Block.

Mesozoic–Cenozoic strata distributed in the Nansha Block (Dangerous Grounds or Spratly Islands) of the southern SCS show
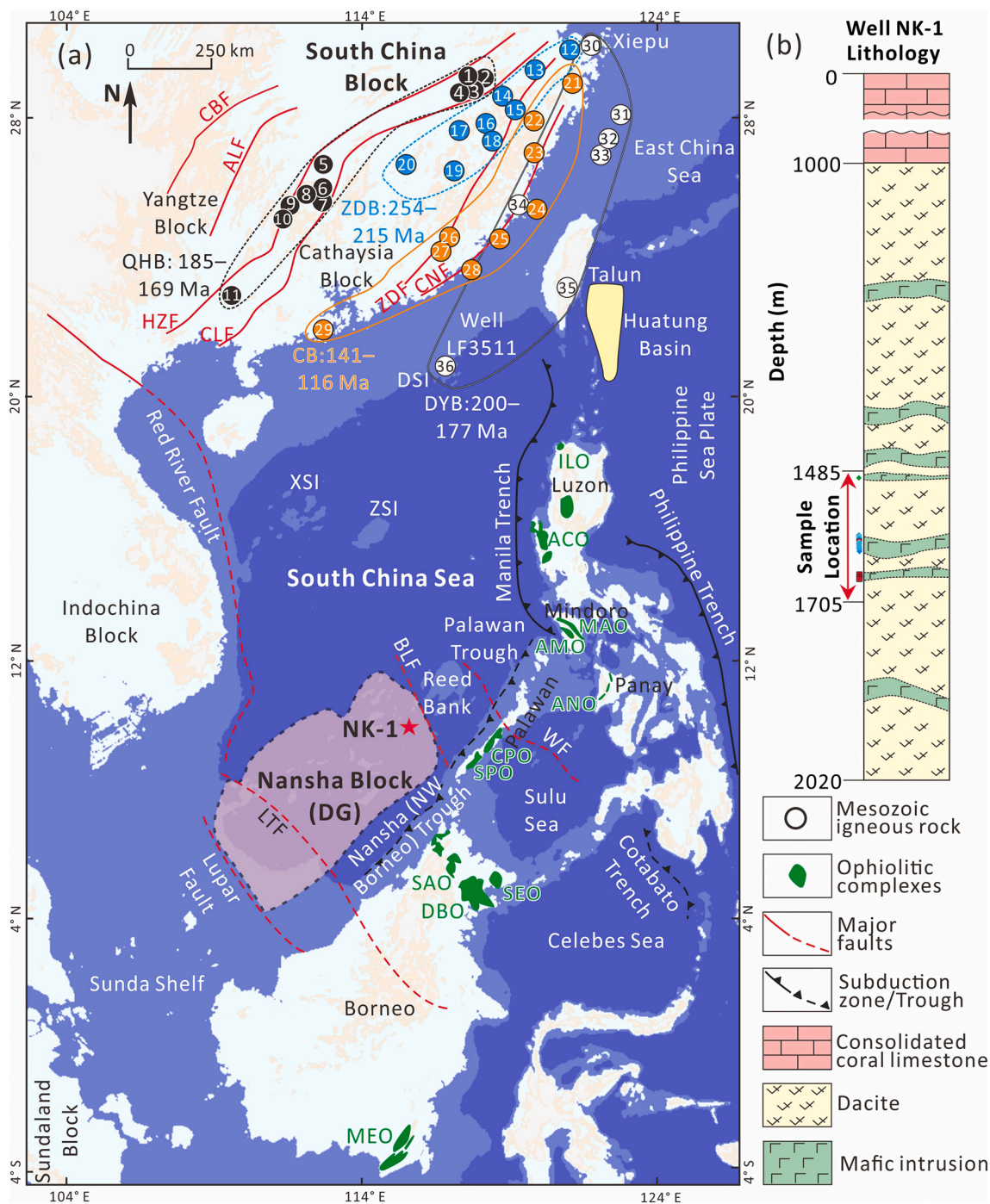
Fig. 1. (a) Simplified tectonic outline of the South China Block and the South China Sea, showing the location of Well NK-1 in the Nansha Block. (b) Igneous basement lithology of Well NK-1. Abbreviations: Qinhang Belt (QHB; the black dotted line); Zhenghe-Dapu Belt (ZDB; the blue dotted line); Coastal Belt (CB; the orange line); DongSha–Talun–Yandong Belt (DYB; the gray line); Anhua–Luocheng Fault (ALF); Balabac Fault (BLF); Changle–Nanao Fault (CNF); Cili–Baojing Fault (CBF); Jiangshan–Shaoxing Fault (JSF); Lizhun–Tinjia Fault (LTF); Qiyueshan Fault (QYF); Wulugen Fault (WF); Xiangfan–Guangji Fault (XGF); Zhenghe–Dapu Fault (ZDF); Dongsha Islands (DSI); Xisha Islands (XSI); Zhongsha Islands (ZSI); Central Palawan ophiolite (CPO); Southern Palawan ophiolite (SPO); Antique ophiolite (ANO); Darvel Bay ophiolite (DBO); Amnay ophiolite (AMO); Ilocos ophiolite (ILO); Mangyan ophiolite (MAO); Acoje ophiolite (ACO); Coto ophiolite (COO); Segama ophiolite (SEO); Meratus ophiolite (MEO) and Sabah ophiolite (SAO). References for the Mesozoic igneous rocks are listed in Appendix 1. (For interpretation of the references to colour in this figure legend, the reader is referred to the web version of this article.)

tectonic affinities with those in the SCB, suggesting that the Nansha Block moved to its present position with the expansion of the SCS or PSCS (Miao et al., 2021). Thus, the Nansha Block may record magmatic activity related to the formation of the PSCS and the tectonic evolution of Southeast Asia since the Mesozoic. In this paper, we present ^{40}Ar/^{39}Ar dating results and whole-rock elemental and Sr–Nd–Hf–Pb isotopic data for mafic igneous rocks from Well NK-1 (NK-1 drillhole) in the Nansha Block (Fig. 1) to investigate the petrogenesis and source characteristics of these rocks. Combining the new results with existing information on Mesozoic igneous rocks in the SCB and ophiolites in the Borneo Block and other microblocks (e.g., the Palawan, Mindoro, and Panay microblocks) in the western Philippines (Fig. 1a), we outline the transition of the Mesozoic tectonic setting in the southern margin of the SCS and its relationship to the opening and spreading of the PSCS.

2. Geological background and sample descriptions

The SCS is a basin bordered by the SCB to the north, the Indochina Block to the west, the Borneo Block to the southwest, the Luzon Block to the east, and the Palawan–Mindoro Block to the south (Fig. 1a). The SCS can be divided into three parts according to lithosphere type: northern continental margin; oceanic basin; and southern continental margin (Fig. 1a). The northern margin of the SCS consists of the Pearl River Mouth Basin, Zhongsha (Macclesfield Bank), Xisha (Paracel Islands), and Dongsha (Pratas Reef). The southern margin of the SCS, including the Nansha and Palawan–Mindoro blocks and Reed Bank, was located along the southern continental margin of the SCB during the Triassic to Late Cretaceous (Miao et al., 2021). As evidence for this configuration, the Triassic dacites from Well NK-1 in the Nansha Block show geochemical affinities with Triassic A-type granites distributed along the Zhenghe–Dapu Fault in the SCB (Fig. 1a), and the detrital zircons from microblocks in the southern SCS margin all have age peaks resembling the age distribution of continental margin basement of the SCB (ca. 1841, 430, 228, and 128 Ma; Miao et al., 2021). This is further identified by the Upper Triassic deltaic sandstones from the Nansha Block, which contain the Dictyophyllum–Clathropteris flora and thus might be originated from the Cathaysia Block (Kudrass et al., 1986). Therefore, the microblocks distributed in the southern SCS were separated from the SCB and gradually drifted southeastward to their present locations during seafloor spreading in the PSCS and SCS (Hall, 2012; Shao et al., 2017; Suggate et al., 2014). During the Cenozoic, the southern margin of the SCS has undergone subduction of the PSCS crust beneath the Borneo Block, as well as collision between the Nansha and Borneo blocks (Hall, 2012). The Nansha Block has an average crust thickness of ~24 km, a width of >400 km, and an area of ~600,000 km^2 (Yan et al., 2010). Since the Mesozoic, the Nansha Block has undergone various tectonic events, including continental lithosphere extension, crustal break-up, seafloor spreading, and collision with Borneo (Cullen, 2010; Larsen et al., 2018). Thus, the Nansha Block is an ideal region for investigating the Mesozoic–Cenozoic tectonic evolution of the SCB, PSCS, and SCS.

Well NK-1 in the Nansha Block has a total depth of 2020.2 m and penetrates coralline limestone (~1000 m) and underlying igneous rocks (~1000 m; Fig. 1b). The drilled igneous rocks are predominantly dacites, with subordinate mafic rocks, including diorites and diabases, which intrude the dacites (Fig. 1b). The studied samples, including diorites and diabases, were collected at a depth range of 1485–1705 m (Fig. 1b).

The diorite samples show inequigranular texture and consist mainly
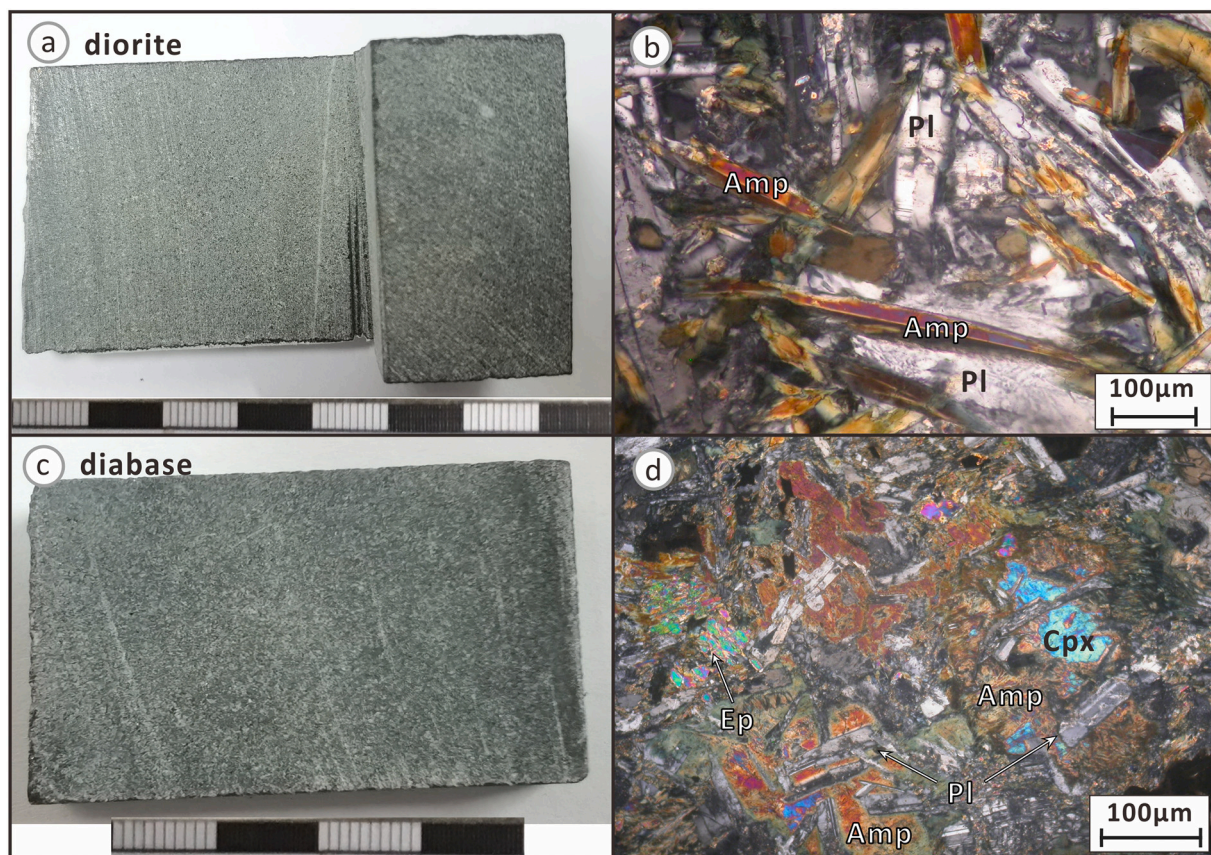
Fig. 2. Petrography of diorites and diabases from Well NK-1. (a) Photograph of diorite sample. (b) Photomicrograph of diorite showing inequigranular texture characterized by elongate laths of amphibole and plagioclase (cross-polarized light). (c) Photograph of diabase sample. (d) Photomicrograph of diabase showing ophitic texture characterized by small crystals of tabular plagioclase partially enclosed in large crystals of clinopyroxene and amphibole (cross-polarized light). Mineral abbreviations: amphibole (Amp), clinopyroxene (Cpx), epidote (Ep), plagioclase (Pl).

of euhedral–subhedral amphiboles (40–45 vol%) and sub-hedral–anhedral plagioclases (55–60 vol%). The amphiboles show variable grain sizes with crystal lengths of ~100–500 μm, and the plagioclases exhibit similar grain sizes with crystal lengths of ~200 μm (Fig. 2a–b). The diabase samples consist of subhedral–anhedral clino-pyroxenes (~20 vol%), euhedral–subhedral plagioclases (~45 vol%), and subhedral–anhedral amphiboles (~35 vol%; Fig. 2c–d). The clino-pyroxenes commonly show irregular rims owing to their replacement of amphiboles. The plagioclases occur mostly as inclusions in clinopyrox-enes or amphiboles and show ophitic texture. Some of the amphiboles and clinopyroxenes have been epidotized (Fig. 2d).

3. Analytical methods

Chronological, geochemical, and isotopic analyses of samples in this study were all carried out at the State Key Laboratory of Isotope Geochemistry (SKLaBIG), Guangzhou Institute of Geochemistry, Chinese Academy of Sciences (GIGCAS).

3.1. $^{40}Ar/^{39}Ar$ dating

For $^{40}Ar/^{39}Ar$ dating, the rock was sawed into slabs and the central part was used. After crushed into 40–60 mesh size in a steel mortar with all phenocrysts removed under a binocular, the sample was cleaned with acetone followed by further cleaning with deionized water in an ultra-sonic bath. The cleaned sample was then dried at 80 °C. Each sample was wrapped in aluminum foil and sealed in a quartz ampoule that was evacuated afterward before being irradiated for 90 h in the Mianyang reactor (Sichuan, China). The J–values for the samples were determined by ZBH-2506 Biotite (132 Ma) flux monitors. In order to obtain J–values for the samples, the monitor ZBH-2506 was packed between every four samples in quartz tubes, each tube containing 4 packets of ZBH-2506. Based on the J–values and the positions of ZBH-2506 in the sample tube, a regression line was obtained for each sample tube, and then the J-values of the samples were calculated by interpolation from the regression line. The J-value uncertainty of 0.15% (1r) was considered in the reported ages. The $^{40}Ar/^{39}Ar$ dating was carried out by Argus VI mass spectrometer. Argon gas was extracted from the sample by step–heating (50 s per step) using a MIR10 CO_2 continuing laser. The background of the sample hold is lower than 2 mV pre-experiment and 4–6 mV during the experiment (after 5 min vacuumize), while the signal of the sample is mostly controlled within the range of 40–200 mV. The Ar-Ar-CALC program (v.2.2; Koppers, 2002) was used for data reduction and age calculation.

3.2. Whole-rock major and trace element analyses

The samples for whole-rock major and trace element analyses were firstly examined using optical microscopy. The selected samples were broken into small chips and cleaned ultrasonically in distilled water containing <3% HNO_3 and washed with distilled water before being dried and handpicked to remove visible contamination. The rocks were powdered before analysis of major and trace elements and were determined by Rigaku RIX 2000 X-ray fluorescence spectrometer (XRF) with analytical uncertainties <5% and inductively coupled plasma–mass spectrometry (ICP-MS), respectively (Li et al., 2006). Trace element concentrations were calibrated using USGS and Chinese National standards AGV-2, GSR-1, GSR-2, GSR-3, BHVO-2, W-2a and SARM-4 with the resulting REE and other incompatible element concentrations typically having analytical precisions of <3%.

3.3. Whole-rock Sr–Nd–Pb–Hf isotope analyses

Sr and Nd isotope analyses were performed using a Neptune Plus multi-collector ICP-MS (MC-ICP-MS). Analytical procedures are identical to those described by Wei et al. (2002) and Li et al. (2004).

Reference standards were analyzed along with samples and gave $^{87}Sr/^{86}Sr$ = 0.710241 ± 10 (2σ) for NBS987 and $^{143}Nd/^{144}Nd$ = 0.512113 ± 8 (2σ) for Shin Etsu JNdi-1, which are comparable to the recommended values of NBS987 ($^{87}Sr/^{86}Sr$ = 0.710248; McArthur, 1994) and Shin Etsu JNdi-1 ($^{143}Nd/^{144}Nd$ = 0.512115 ± 7; Tannaka et al., 2000). For Pb isotopic determination, about 100 mg powder per sample was weighed into the Teflon beaker, then spiked and dissolved in concentrated HF at 180 °C for 7 h. Lead was separated and purified by the conventional cation–exchange technique (AG1 × 8, 200–400 resin) with diluted HBr as an eluant. Total procedural blanks were less than 50 pg Pb. Isotopic ratios were measured using a VG-354 mass-spectrometer following procedures described by Baker et al. (2004). Repeated analyses of SRM 981 yielded average values of $^{206}Pb/^{204}Pb$ = 16.900 ± 4 (2σ), $^{207}Pb/^{204}Pb$ = 15.498 ± 4 (2σ) and $^{208}Pb/^{204}Pb$ = 36.728 ± 9 (2σ).

Whole-rock Hf isotopic ratios were measured using a Neptune Plus MC-ICP-MS. The samples for Hf isotopic analysis were digested using alkali fusion method. The mixture with 0.5 g rock powder and 1.0 g $Li_2B_4O_7$ was digested for 15 min at 1100 °C in 95% Pt–5% Au crucibles in a high-frequency furnace. The quenched piece of alkali glass was then dissolved by 2 M HCl. The sample was loaded on a column that contained Ln-Spec in 2 M HCl and separated using a modified single–column separation procedure (Li et al., 2006). Reference standard JMC14374 was analyzed along with samples and gave $^{176}Hf/^{177}Hf$ = 0.282159 ± 8 (2σ), which is consistent with the recommended value ($^{176}Hf/^{177}Hf$ = 0.0.282151 ± 7; Woodhead and Hergt, 2005).

4. Results

4.1. $^{40}Ar/^{39}Ar$ ages

The $^{40}Ar/^{39}Ar$ dating results for plagioclases from diorite (sample NK-1-V$_3$-094, depth 1617 m) and diabase (sample NK-1-V$_3$-004, depth 1503 m) from Well NK-1 are given in Supplemental Table 1, and the age spectra of $^{40}Ar/^{39}Ar$ dating results are presented in Fig. 3. All age determinations define statistically acceptable plateau (Fig. 3a, c), comprising 70%–80% of the gas released with trapped $^{40}Ar/^{36}Ar$ ratios (314 ± 10 and 312 ± 3 for the respective samples) that are similar to the atmospheric $^{40}Ar/^{36}Ar$ ratio of 295.5 (Fig. 3b, d; Steiger and Jäger, 1977). Sample NK-1-V$_3$-094 shows the plateau age of 177 ± 12 Ma, similar to its normal isochron age (180 ± 24 Ma) and inverse isochron age (180 ± 28 Ma), which is interpreted as the crystallization age of the diorites. Sample NK-1-V$_3$-004 has the plateau age of 124 ± 5 Ma, consistent with the normal isochron age of 128 ± 13 Ma and inverse isochron age of 128 ± 13 Ma (Fig. 3) within errors, which is interpreted as the crystallization age of the diabases.

4.2. Whole-rock major- and trace-element compositions

Whole-rock major- and trace-element compositions of the diorite and diabase samples from Well NK-1 are provided in Supplemental Table 2. Given that the studied samples have relatively high loss-on-ignition values (LOI = 1.04–3.49 wt%), the major elements were recalculated on an anhydrous basis.

The diorite samples show basaltic–andesitic composition and have narrow ranges of SiO_2 (53.6–55.9 wt%), Na_2O (2.76–3.02 wt%), and K_2O (0.46–1.14 wt%) contents, with total alkalis (Na_2O + K_2O) of 3.48–3.90 wt%, (Fig. 4a). They also exhibit narrow ranges of MgO (3.32–4.22 wt%) and Fe_2O_3 (9.28–10.4 wt%) contents with low $Mg^{\#}$ values (100 × Mg/[Mg + Fe^{2+}]; 41.2–44.9) and relatively high FeO^{Tot}/MgO ratios (2.18–2.57), indicative of tholeiitic series (Fig. 4b). In comparison with the diorite samples, the diabase samples contain lower SiO_2 (48.9–50.1 wt%), higher MgO (6.13–7.92 wt%) and Fe_2O_3 (12.9–14.4 wt%) and similar Na_2O (2.69–3.28 wt%) and K_2O (0.41–1.77 wt%) contents, with total alkali contents of 3.46–4.06 wt%, corresponding to basalt in a total-alkali–silica (TAS) diagram (Fig. 4a). In addition, the diabase samples have higher $Mg^{\#}$ values (45.7–54.3)
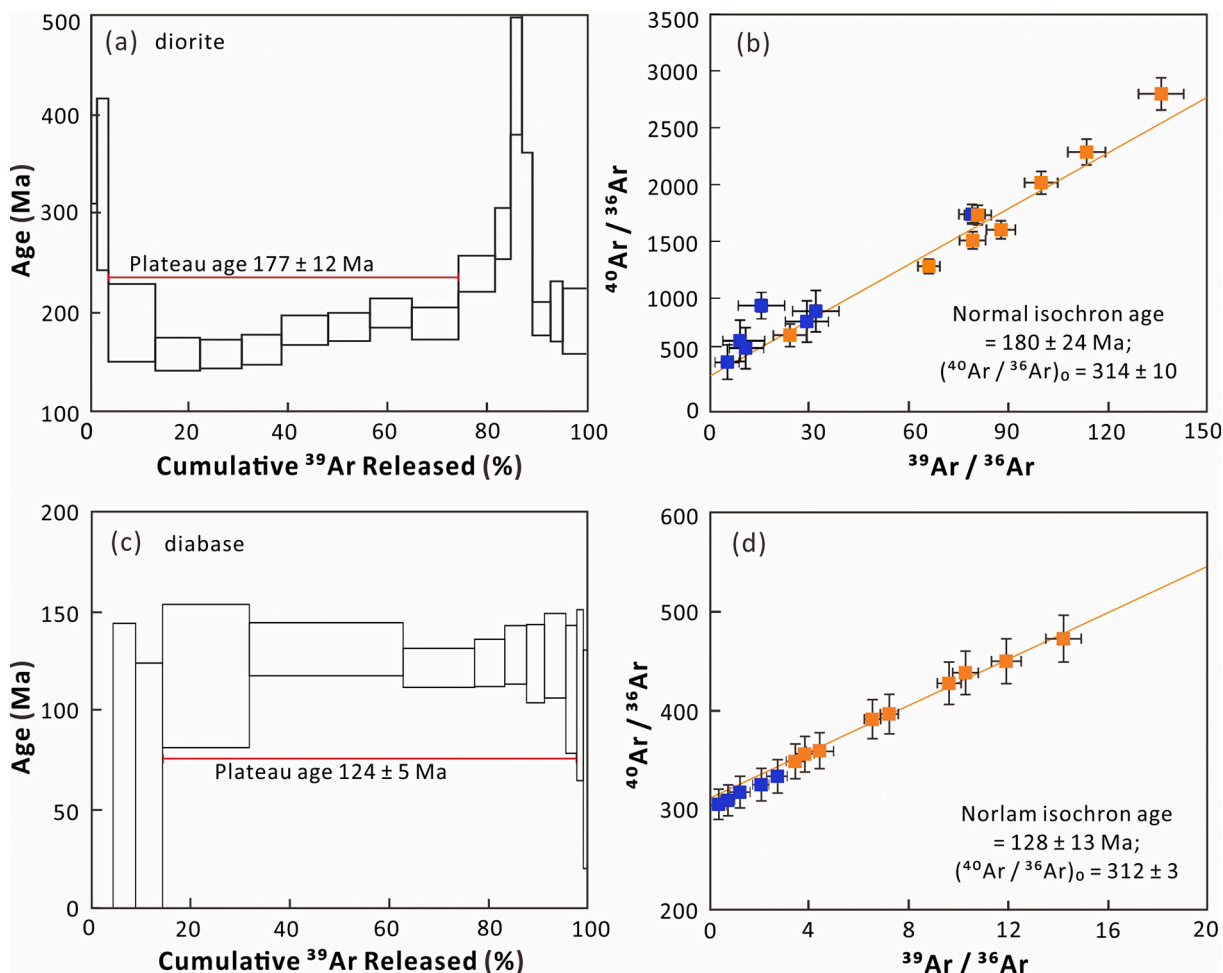
Fig. 3. $^{40}Ar/^{39}Ar$ plateau age spectra and trapped $^{40}Ar/^{36}Ar$ ratios for the diorite and diabase samples from Well NK-1. (a, b) Diorite sample NK-1-V$_3$-094, (c, d) diabase sample NK-1-V$_3$-004.
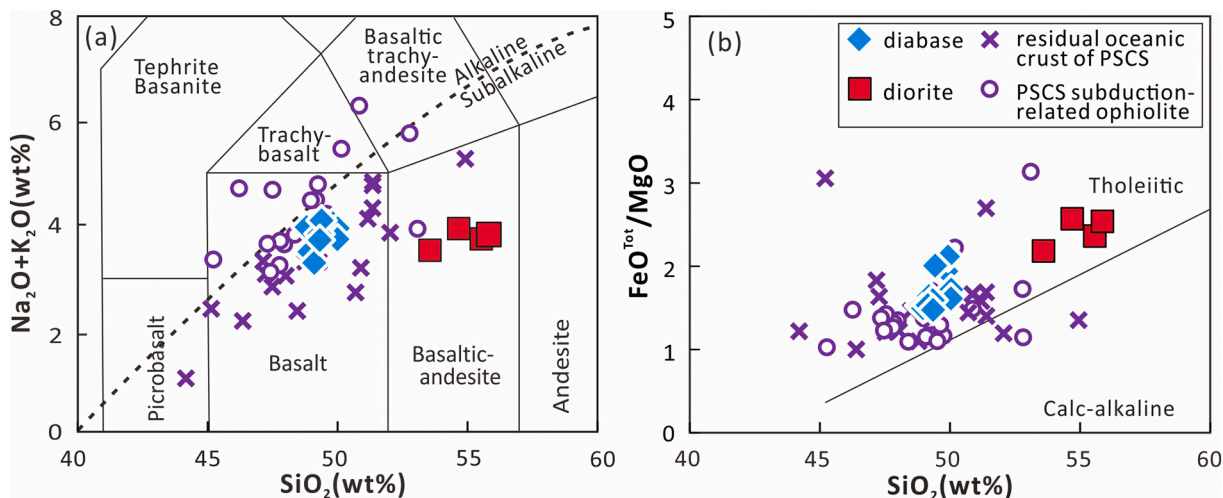

Fig. 4. Diagrams of (a) TAS (data calculated on a volatile-free basis; Le Maitre, 1989), and (b) FeO^{Tot}/MgO vs. SiO$_2$ for diorite and diabase samples from Well NK-1. Data for ophiolites and mafic intrusions regarded as remnants of oceanic crust of the PSCS are from Hickey-Vargas et al. (2008), Gibaga et al. (2020), Tamayo et al. (2001), and Omang and Barber (1996); data for PSCS subduction-related ophiolites are from Yu et al. (2020).

and lower FeO^{Tot}/MgO ratios (1.48–2.12) compared with the diorite samples and are classified as tholeiitic (Fig. 4b).

The diorite samples show fractionated rare earth element (REE) patterns ([La/Yb]$_N$ = 1.99–3.89; N = chondrite-normalized values),

with flat heavy REEs ([Dy/Yb]$_N$ = 1.04–1.09) and slight positive Eu anomalies (Eu/Eu* = 1.10–1.29; Fig. 5a; Supplemental Table 2). They are enriched in fluid-mobile elements (e.g., Rb, Ba, Pb, and Sr) and depleted in Nb, Ta, and Ti relative to normal mid-ocean ridge basalt (N-
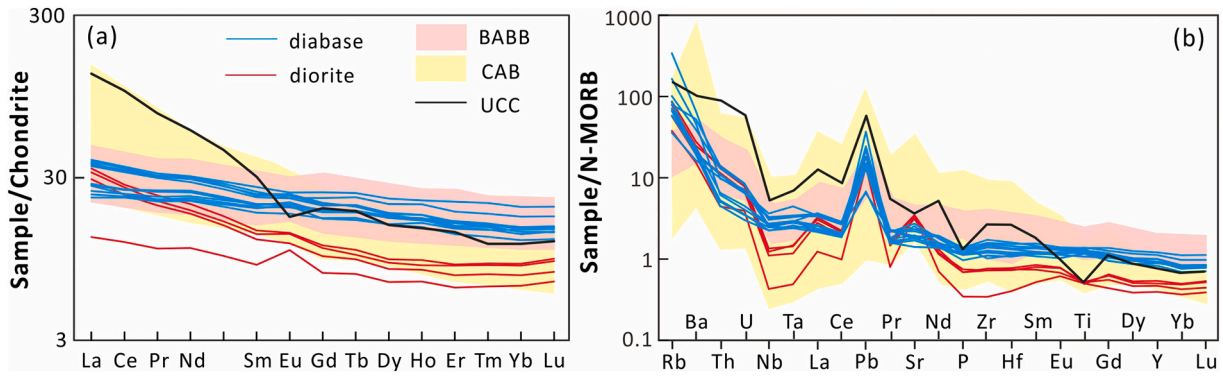
Fig. 5. Diagrams of (a) chondrite-normalized REE patterns and (b) N-MORB normalized trace-element variations for diorite and diabase samples from Well NK-1. Normalization values are from Sun and McDonough (1989). CAB data are for Mexico and Cascades continental arc basalts (Schmidt and Jagoutz, 2017). BABB data are for Okinawa Trough and Japan basalts (Hirahara et al., 2015; Hoang and Uto, 2006).

MORB; Sun and McDonough, 1989), resembling continental arc basalt (CAB; Fig. 5b). In comparison, the diabase samples are characterized by slightly fractionated light REE patterns ([La/Yb]$_N$ = 1.63–2.59), with flat heavy REEs ([Dy/Yb]$_N$ = 1.08–1.26) and negligible Eu anomalies (Eu/Eu* = 0.95–1.10; Fig. 5a; Supplemental Table 2). Furthermore, the diabase samples are enriched in Rb, Ba, Pb, and Sr and show negligible to slight positive or negative Nb, Ta, Ti, Zr, and Hf anomalies, being

geochemically similar to back-arc basin basalt (BABB; Fig. 5b).

4.3. Whole-rock Sr–Nd–Pb–Hf isotope compositions

Whole-rock Sr–Nd–Pb–Hf isotopic results for the studied samples from Well NK-1 are given in Supplemental Table 2. The ratios of (^{87}Sr/^{86}Sr)$_i$, (^{206}Pb/^{204}Pb)$_i$, (^{207}Pb/^{204}Pb)$_i$, and (^{208}Pb/^{204}Pb)$_i$ (where
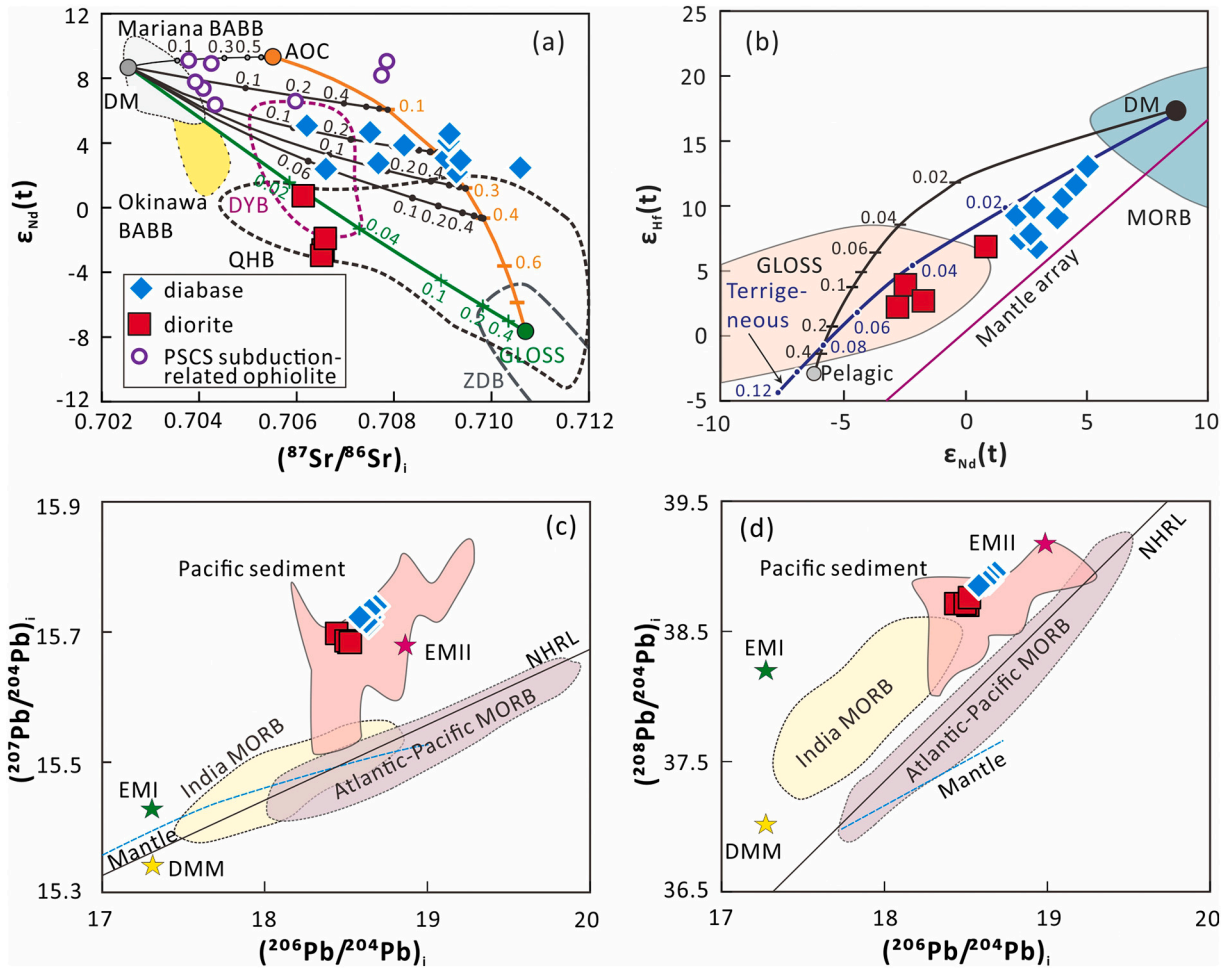
Fig. 6. Diagrams of (a) ε$_{Nd}$ vs. (^{87}Sr/^{86}Sr)$_i$, (b) ε$_{Hf}$(t) vs. ε$_{Nd}$(t), (c) (^{207}Pb/^{204}Pb)$_i$ vs. (^{206}Pb/^{204}Pb)$_i$, and (d) (^{208}Pb/^{204}Pb)$_i$ vs. (^{206}Pb/^{204}Pb)$_i$ for diorite and diabase samples from Well NK-1. Ratios of (^{87}Sr/^{86}Sr)$_i$ and values of ε$_{Nd}$(t) and ε$_{Hf}$(t) for DM, AOC, GLOSS, and pelagic and terrigenous sediments were calculated at 124 Ma and are given in Supplemental Table 3. The Nd—Hf isotopic mantle array (ε$_{Hf}$ = ε$_{Nd}$ × 1.59 + 1.28) is from Chauvel et al. (2008). Pb isotopic data for DM, EMI, and EM II are from Workman and Hart (2005) and Iwamori and Nakamura (2015). The Northern Hemisphere Reference Line (NHRL) is from Hart (1984).

subscript "i" signifies initial ratios) and values of $\varepsilon_{Nd}(t)$ and $\varepsilon_{Hf}(t)$ for the diorite and diabase samples were calculated at 177 and 124 Ma, respectively.

The diorite samples have relatively low $^{87}Sr/^{86}Sr$ (0.70657–0.70748), $^{143}Nd/^{144}Nd$ (0.51243–0.51264), and $^{176}Hf/^{177}Hf$ ratios (0.28280–0.28297), corresponding to relatively low $(^{87}Sr/^{86}Sr)_i$ ratios (0.70607–0.70645; Fig. 6a) and $\varepsilon_{Nd}(t)$ (−2.8 to +0.8) and $\varepsilon_{Hf}(t)$ (+2.2 to +6.9) values (Fig. 6b). The samples display a narrow range of Pb isotopic compositions ($^{206}Pb/^{204}Pb = 18.579–18.633$, $^{207}Pb/^{204}Pb = 15.688–15.703$, and $^{208}Pb/^{204}Pb = 38.806–38.935$, respectively) with

$(^{206}Pb/^{204}Pb)_i$, $(^{207}Pb/^{204}Pb)_i$, and $(^{208}Pb/^{204}Pb)_i$ ratios of 18.443–18.529, 15.684–15.698, and 38.730–38.789, respectively (Fig. 6c, d).

The diabase samples exhibit variable $^{87}Sr/^{86}Sr$ (0.70804–0.72014; Fig. 6a) and a wide range of $(^{87}Sr/^{86}Sr)_i$ ratios (0.70654–0.71235). However, they have narrow ranges of $^{143}Nd/^{144}Nd$ (0.51272–0.51288) and $^{176}Hf/^{177}Hf$ (0.28294–0.28313) ratios, corresponding to positive $\varepsilon_{Nd}(t)$ (+2.1 to +5.0) and $\varepsilon_{Hf}(t)$ (+7.5 to +11.6) values (Fig. 6b). The diabase samples have a narrow range of Pb isotopic compositions ($^{206}Pb/^{204}Pb = 18.643–18.789$, $^{207}Pb/^{204}Pb = 15.683–15.741$, and

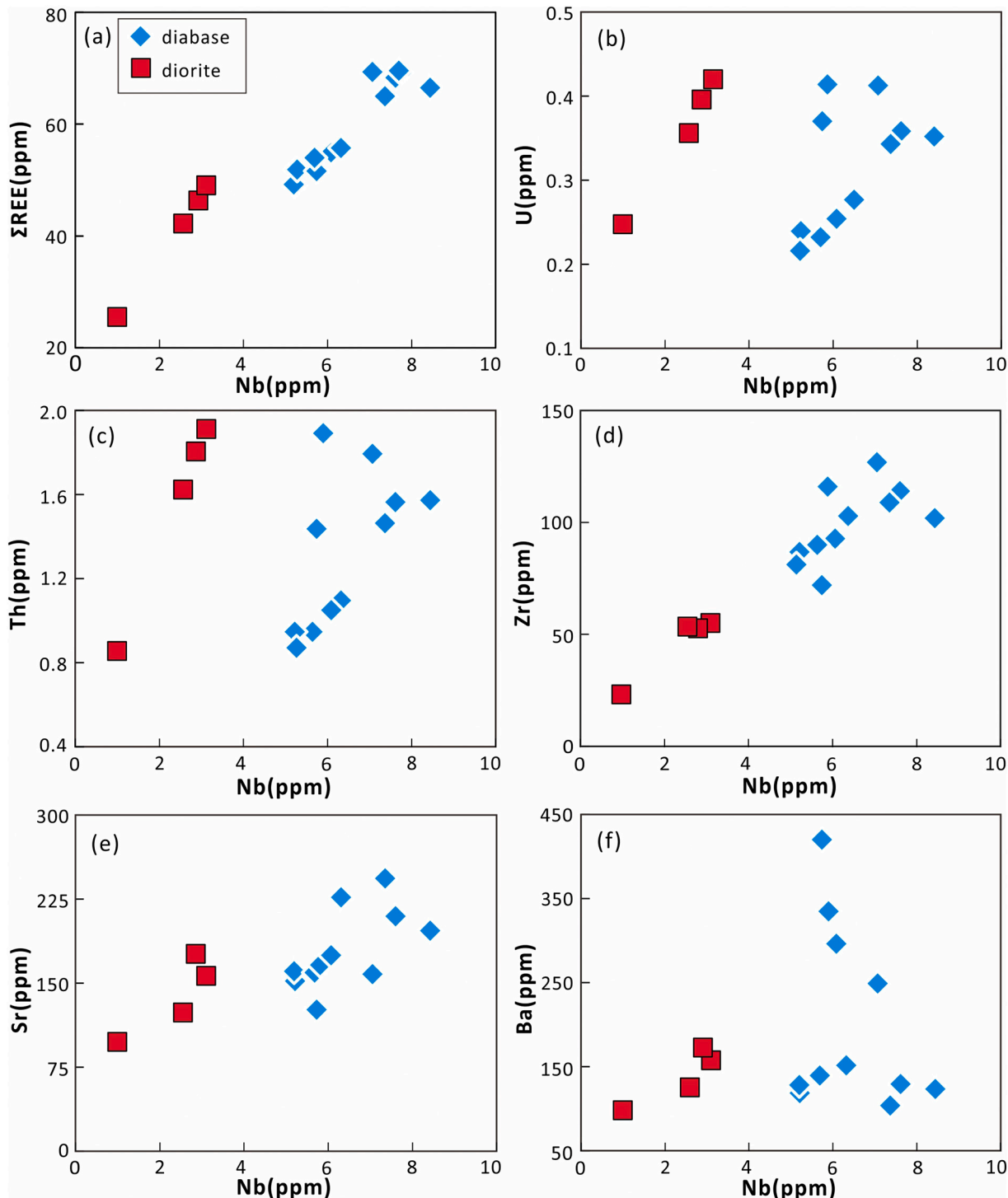**Fig. 7.** Plots of (a) ΣREE vs. Nb, (b) U vs. Nb, (c) Th vs. Nb, (d) Zr vs. Nb, (e) Sr vs. Nb and (f) Ba vs. Nb, for diorite and diabase samples from Well NK-1.

^{208}Pb/^{204}Pb = 38.914–39.108), corresponding to (^{206}Pb/^{204}Pb)$_i$, (^{207}Pb/^{204}Pb)$_i$, and (^{208}Pb/^{204}Pb)$_i$ ratios of 18.584–18.683, 15.715–15.739, and 38.885–38.985, respectively (Fig. 6c, d).

5. Discussion

5.1. Effects of alteration, crustal contamination, and fractional crystallization on rock compositions

The presence of alteration minerals such as epidote (Fig. 2d) indicates that the samples from Well NK-1 might have undergone varying degrees of alteration after emplacement, consistent with their variable
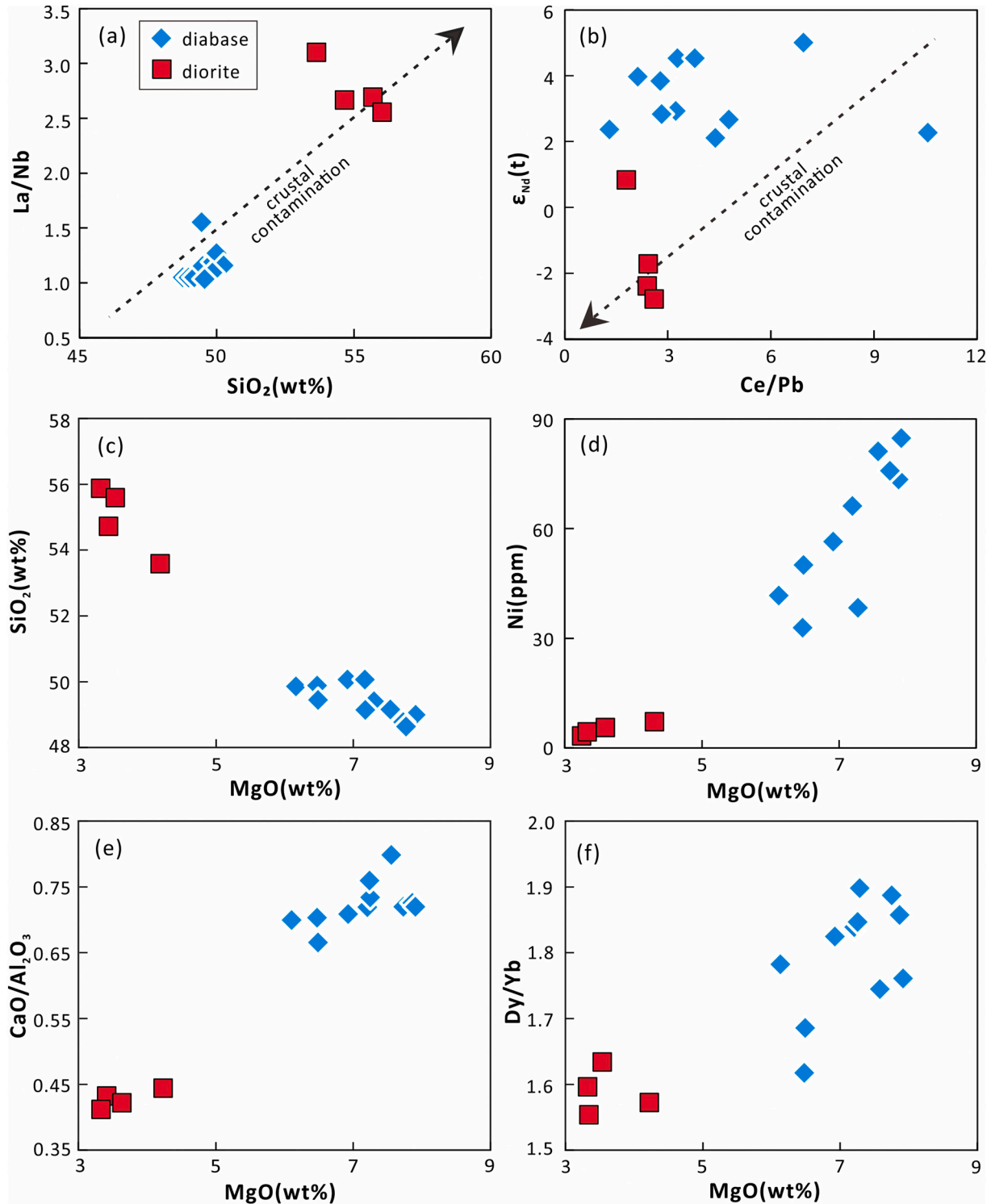

Fig. 8. Plots of (a) La/Nb vs. SiO$_2$, (b) ε$_{Nd}$(t) vs. Ce/Pb, (c) SiO$_2$ vs. MgO, (d) Ni vs. MgO, (e) CaO/Al$_2$O$_3$ vs. MgO and (f) Dy/Yb vs. MgO for diorite and diabase samples from Well NK-1.

LOI values (1.04–3.49 wt%). Large-ion lithophile elements (LILEs; e.g., Sr, Rb, and Ba) and REEs are readily influenced by alteration (Patino et al., 2004). In contrast, high-field-strength elements (HFSEs; e.g., Nb and Zr) are usually immobile during low-grade metamorphism and alteration, and thus relationships between Nb and other elements can be used to evaluate whether these elements have been affected by alteration (Polat and Hofmann, 2003). The diorite samples show positive relationships between Nb and total REEs (ΣREE), U, Th, Zr, Ba, and Sr (Fig. 7a–f), indicating that these elements have not been substantially influenced by alteration. The diabase samples also show positive relationships between Nb and ΣREE, U, Th, Zr, and Sr (Fig. 7a–e), but not with Ba (Fig. 7f). Thus, except for some LILEs, most elements in the diabase samples were not or only negligibly influenced by alteration.

Mantle-derived melts will inevitably be affected by crustal contamination to some degree during their ascent through the crust and by evolution within magma chambers in the crust. The diorite samples show characteristics that are usually indicative of crustal contamination, such as enriched Sr–Nd–Hf–Pb isotopes (Fig. 6) and negative Nb–Ta–Ti anomalies (Fig. 5b). However, the diorite samples also exhibit positive Sr anomalies and negligible Zr and Hf anomalies (Fig. 5b), which may argue against the crustal influence on compositions. Furthermore, the crustal contamination would enhance SiO_2 contents and La/Nb ratios but reduce Ce/Pb ratios and $\varepsilon_{Nd}(t)$ values of the melts, because the crustal materials generally have high La and Pb relative to Nb and Ce, with high SiO_2 contents and relatively low $\varepsilon_{Nd}(t)$ values (Rudnick and Gao, 2003). The diorite samples show negative correlations on the diagrams of La/Nb versus SiO_2 and Ce/Pb versus $\varepsilon_{Nd}(t)$ (Fig. 8a–b), which are obviously in contradiction with the crustal contamination. Thus, the crustal signature in the diorite samples cannot be attributed to crustal contamination but might have been derived from the mantle source. This explanation is further supported by the higher Nb/Ta ratios (15.0–16.6) of the diorite samples relative to crust (8.33–13.3, Rudnick and Gao, 2003). Crustal contamination is also negligible for the diabases because the samples show negligible to slight Nb, Ta, Ti, Zr, and Hf anomalies (Fig. 5b) and have overall depleted Nd and Hf isotopes (Fig. 6a–b), with low La/Nb ratios (1.01–1.55; Supplemental Table 2).

In general, mantle-derived primary melts have Ni > 400 ppm, Cr > 1000 ppm, and $Mg^{\#}$ = 73–81 (Litvak and Poma, 2010). The diabase samples have relatively low and variable $Mg^{\#}$ (45.7–54.3), Cr (42.7–234 ppm), and Ni (32.3–85.0 ppm; Supplemental Table 2) and show a negative relationship between SiO_2 and MgO (Fig. 8c), indicating substantial fractionation of mafic minerals (e.g., olivine, clinopyroxene, and amphibole) during magma evolution. The fractionation of olivine, clinopyroxene, and amphibole for the diabase samples is further evidenced by positive relationships between MgO and Ni, CaO/Al_2O_3, and Dy/Yb, respectively (Fig. 8c–f). The diorite samples also show a negative relationship between SiO_2 and MgO (Fig. 8c) but have much lower $Mg^{\#}$ (41.2–44.9), Cr (6.36–16.1 ppm), and Ni (0.91–5.47; Supplemental Table 2) compared with the diabase samples, indicating a higher degree of fractionation of mafic minerals during magma evolution and/or derived from a less primary melt. Amphibole, which constitutes the main phenocrysts in the diorite samples (Fig. 2b), could be a fractionation phase. Furthermore, both the diabase and diorite samples show fractionated REE patterns without negative Eu anomalies (Fig. 5a), excluding significant fractionation of plagioclase.

5.2. Petrogenesis of Mesozoic mafic rocks of the Nansha Block

The diorite samples are basaltic–andesitic in composition with low SiO_2 contents (53.6–55.9 wt%), together with the positive $\varepsilon_{Hf}(t)$ values of +2.2 to +6.9 (Figs. 4a and 6b), which indicates the derivation from the mantle source rather than from the crustal source. Furthermore, the diorite samples have similar Nb/Ta ratios (14.9–16.7) to those of MORB (Nb/Ta = 9.29–16.8; Chauvel and Blichert-Toft, 2001), indicating an origin dominated by depleted asthenospheric mantle. Therefore, the CAB-like features of the diorite samples, such as enrichment in LREEs,

Ba, Pb, and Sr and negative Nb, Ta, and Ti anomalies (Fig. 5), are interpreted to have resulted from interaction between the mantle wedge and aqueous fluids and/or melts released from the subducted slab (i.e., oceanic crust and overlying sediments; Woodhead et al., 2001). Because oceanic crust is generally derived from depleted mantle, fluids and/or melts from the subducted oceanic crust cannot significantly modify the Nd—Hf isotopic compositions of the depleted mantle wedge. Thus, the more enriched Nd–Hf–Pb isotopes of the diorite samples relative to the depleted mantle and their pronounced positive Pb anomalies indicate the input of fluids and/or melts from subducted sediments into the mantle wedge (Figs. 5b and 6). Subducted sedimentary components generally have high Th/Nb ratios (~0.77; Plank and Langmuir, 1998) and low $\varepsilon_{Nd}(t)$ values. The diorite samples from Well NK-1 have high Th/Nb ratios (0.46–0.55) and show a negative relationship between Th/Nb and $\varepsilon_{Nd}(t)$ (Fig. 9a), consistent with a mantle source metasomatized by sediment-derived melts. This interpretation is supported by the decoupled Nd—Hf isotopes of the diorite samples (Fig. 6b). During the partial melting of subducted sediment, zircon, monazite, and rutile are residual phases (Todd et al., 2010; Tollstrup and Gill, 2005). This partial melting process would result in decoupling of Nd—Hf isotopes of the mantle source, with more enriched Nd relative to Hf (Fig. 6b). The diorite samples have low Hf concentrations (0.82–1.58 ppm) and show higher Nd/Hf ratios (5.46–6.20) than depleted mantle (3.56; Sun and McDonough, 1989), which can be achieved by the existence of residual zircon due to high partition coefficient of Hf in zircon. The positive correlation between Nd/Hf and $\varepsilon_{Hf}(t)$ further indicates that the decoupled Nd—Hf isotopes of the diorite samples were caused by zircon residue during the partial melting of subducted sediments (Fig. 9b). This is consistent with their enriched Pb isotopic compositions, which plot in the field of Pacific sediments (Fig. 6c–d). Our model calculation based on Sr–Nd–Hf isotopic compositions shows that the Early Jurassic diorites in the Nansha Block might have been derived from partial melting of a mantle source generated by the addition of a small amount (2%–5%) of subducted sediment (e.g., GLOSS) melts into the depleted asthenospheric mantle (Fig. 6a–b).

The diabase samples exhibit slight enrichment in LREEs, Ba, and Pb, with negligible Nb, Ta, Ti, Zr, and Hf anomalies (Fig. 5), which are similar characteristics to those of BABB. Moreover, the diabase samples plot within the BABB field in diagrams of La/Nb versus Y and TiO_2 versus FeO^{Tot}/MgO (Fig. 10). It is generally recognized that the mantle source for BABB is derived from the interaction between depleted asthenospheric mantle and subducted materials (Gribble et al., 1998; Stern et al., 1990). The diabase samples have depleted Nd—Hf isotopic compositions, with positive $\varepsilon_{Nd}(t)$ (+2.2 to +5.1) and $\varepsilon_{Hf}(t)$ (+7.1 to +11.9) values, which suggest a depleted mantle source (Fig. 6b). However, the diabase samples contain even more enriched Pb isotopes than the diorite samples, which were derived from the partial melting of mantle source influenced by the subducted sediments (Fig. 6c–d). This indicates that the mantle source for the diabase samples might involve the fluids and/or melts released from subducted sediments. The fluids released from subducted sediments are usually enriched in Rb, K, Sr, Ba, Pb, and U due to high mobility of LILEs in fluids (Regelous et al., 1997). Thus, the slight enrichment in Pb, Rb, and K of the samples (Fig. 5b) implies that it would be aqueous fluids rather than the melts involved in the mantle source. In addition, the aqueous fluids released from subducted sediments have high Sr/Nd ratios due to the higher solubility of Sr than Nd in aqueous fluids (Regelous et al., 1997). The diabase samples show relatively high Sr/Nd ratios that are negatively corrected with $\varepsilon_{Nd}(t)$ values (Fig. 9c), further indicating the involvement of aqueous fluids released from subducted sediments. This is consistent with low Th/Nb ratios (0.10–0.28; Fig. 9a) and slightly decoupled Nd—Hf isotopes of the diabase samples (Fig. 6b), for which the mantle source was metasomatized by aqueous fluids rather than melts released from subducted sediments. Nevertheless, the diabase samples show a wide range of $(^{87}Sr/^{86}Sr)_i$ ratios (0.70654–0.71235) but a limited variability in $\varepsilon_{Nd}(t)$ values (+2.2 to +5.1), which could not be generated completely
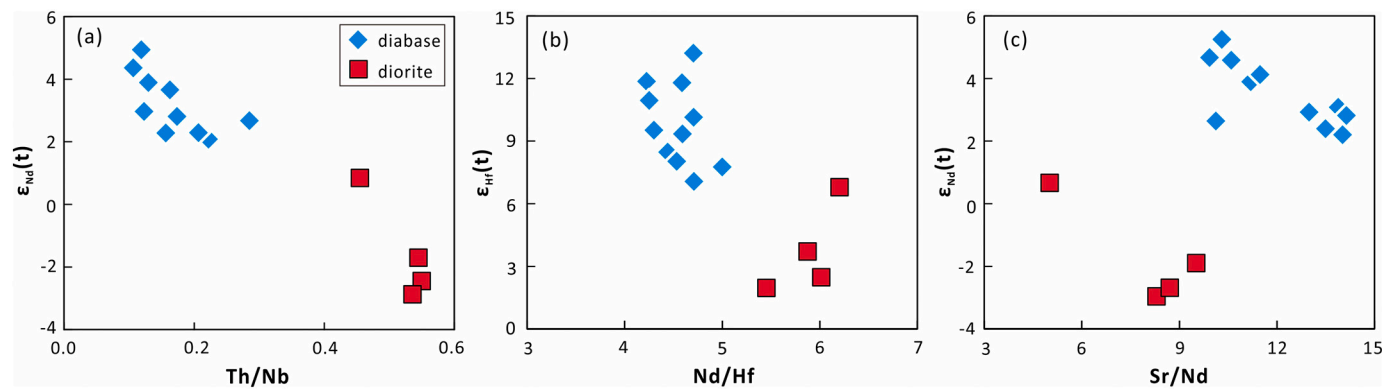
Fig. 9. Plots of (a) $\varepsilon_{Nd}(t)$ vs. Th/Nb, (b) $\varepsilon_{Hf}(t)$ vs. Nd/Hf and (c) $\varepsilon_{Nd}(t)$ vs. Sr/Nd for diorite and diabase samples from Well NK-1.
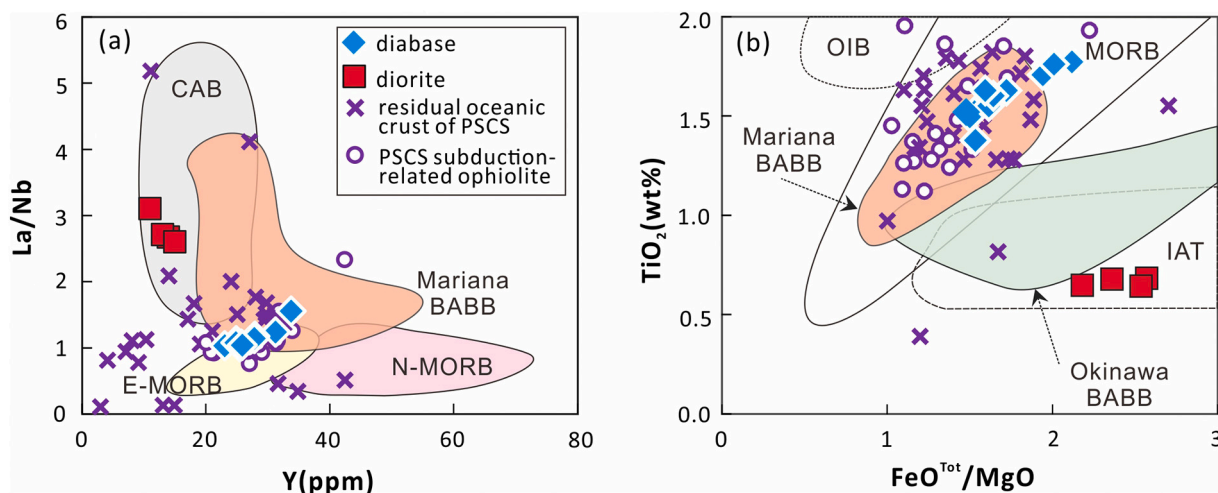

Fig. 10. Diagrams of (a) La/Nb vs. Y (Floyd et al., 1991) and (b) TiO_2 vs. FeO^{Tot}/MgO (Shuto et al., 2006) for diorite and diabase samples from Well NK-1. Abbreviations: continental arc basalt (CAB); enriched mid-ocean ridge basalt (E-MORB); normal mid-ocean ridge basalt (N-MORB); back-arc basalt (BABB); oceanic island basalt (OIB) and island arc tholeiite (IAT). Data for Okinawa BABB, Mariana BABB, and CAB are from Gribble et al. (1996, 1998), Shinjo et al. (1999), and Schmidt and Jagoutz (2017), respectively.

by a simple mixture of depleted mantle and aqueous fluid released from subducted sediments (Fig. 6a). Because the altered oceanic crust (AOC) displays a wide range of $^{87}Sr/^{86}Sr$ ratios with relatively constant $\varepsilon_{Nd}(t)$ values (Handley et al., 2007), the aqueous fluids and/or melts released from the subducted oceanic crust may have been incorporated into the mantle source of the diabase samples. The melts derived from the subducted oceanic crust generally show geochemical characteristics of adakitic rocks with depleted HREE and high Sr/Y ratios (Wang et al., 2008), which is not observed in the diabase samples. Thus, the additional components incorporated into the mantle source for the diabase samples would be aqueous fluids dehydrated from the altered oceanic crust. This is also supported by the mixing model based on Sr—Nd isotopic compositions, which shows that the diabase samples could have been formed by partial melting of an asthenospheric mantle source with input of aqueous fluids released from the AOC and the overlying sediments (Fig. 6a). Collectively, the Early Cretaceous diabases of the Nansha Block were most likely derived from partial melting of an overall depleted asthenospheric mantle source metasomatized by aqueous fluids released from the subducted slab (i.e., AOC and overlying sediments).

5.3. Tectonic settings of the formation of diorites and diabases from Well NK-1

The southern continental margin of the SCS, including the Nansha,

Palawan–Mindoro blocks and Reed Bank, was attached to the southeastern continental margin of the SCB during the Triassic to Late Cretaceous (Miao et al., 2021). Thus, these microblocks that are presently distributed in the southern SCS would have been affected by Paleo-Pacific plate subduction during the Mesozoic because this subduction had started prior to the Early Triassic (Miao et al., 2021; Shen et al., 2018; Xu et al., 2018). The diorite samples from Well NK-1 show CAB affinities, with high La/Nb, FeO^{Tot}/MgO, and Th/Yb ratios (Figs. 5b, 10 and 11). Furthermore, the old two-stage Nd model ages (2.0–1.4 Ga) of the Triassic dacites (217 Ma) from Well NK-1 and granitoids from the SCB (Gao et al., 2017; Miao et al., 2021) demonstrate the existence of ancient crustal basement, suggesting that the continental margin of the SCB was influenced by continental arc magmatism from the Triassic. Thus, the Early Jurassic diorites (177 ± 12 Ma) from the Nansha Block were formed in a continental arc setting associated with subduction of the Paleo-Pacific plate (Fig. 12a, b). This tectonic configuration is consistent with the NE–SW-trending Dongsha–Talun–Yandang magmatic arc belt along the SCB continental margin (Fig. 1a), which has been identified on the basis of arc-related granites and diorites from Well LF3511 (198–195 Ma; Xu et al., 2017) in the northern SCS and the Xiepu I-type granites (ca. 178 Ma; Zhu et al., 2016) in the eastern SCB (Fig. 1a).

The diabase samples (124 ± 5 Ma) from Well NK-1 are compositionally similar to BABB (Fig. 5b), with low La/Nb and Th/Yb ratios and low TiO_2 contents (Figs. 10 and 11), suggesting a back-arc basin setting during the Early Cretaceous. The Nansha, Palawan, and Mindoro blocks
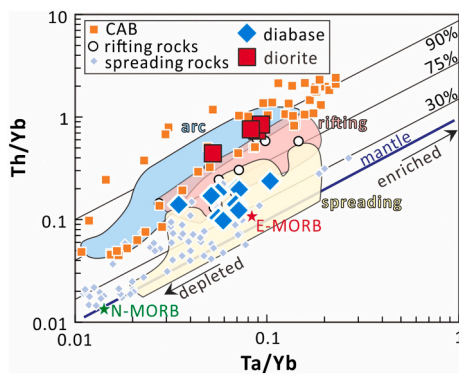
Fig. 11. Diagram of Th/Yb vs. Ta/Yb for diorite and diabase samples from Well NK-1, showing deviations from the MORB array for different contributions (i.e., 30%, 75%, and 90%) of subduction-mobile elements to the mantle source (Pearce et al., 2005). Arc-related rocks are Mexico and Cascades continental arc basalts (Schmidt and Jagoutz, 2017). Mafic rocks associated with the rifting and spreading stages of a back-arc basin are represented by the Caribbean and Mariana BABBs (Pearce et al., 2005; Viruete et al., 2008).

and Reed Bank were attached to the continental margin of the SCB during the Mesozoic (Miao et al., 2021), which was most likely in an extensional setting during the Cretaceous because of retreat and rollback of the subducting Paleo-Pacific slab (Li et al., 2014). For example, 125–90 Ma A-type granites and bimodal magmatic rocks in the coastal area of Fujian province can be explained as products of a back-arc extension setting during the Cretaceous (Li et al., 2014). Therefore, the Early Cretaceous diabases (124 ± 5 Ma) from the Nansha Block might also have been formed in a back-arc basin extensional setting related to retreat and rollback of the subducting Paleo-Pacific plate (Fig. 12c, d).

The evolution of back-arc basins can be divided into three stages, namely, crustal stretching, rifting, and spreading (e.g., Viruete et al., 2008; Yan and Shi, 2014). During the crustal stretching stage, upwelling of asthenospheric mantle under tectonic extension can provide sufficient heat for crustal anatexis to occur. Primitive magma derived from partial melting of the lower continental crust may undergo differentiation to produce dacites or rhyolites. Thus, the crustal stretching stage is typically characterized by highly thinned crust and the occurrence of predominant rhyolite (Yan and Shi, 2014), which is inconsistent with the diabase samples from Well NK-1. From rifting to subsequent spreading of the back-arc basin, magmatic compositions change systematically from early arc-like lavas to later MORB-like basalts (Fig. 11; Pearce et al., 2005; Viruete et al., 2008), owing to the decreasing involvement of crustal materials in the magma source. The diabase samples show low Th/Yb ratios, which indicate a low contribution of subducted materials in the mantle source of these rocks (Fig. 11). In addition, the diabase samples have depleted Nd—Hf isotopic compositions (Fig. 6a–b), further implying their generation during back-arc basin spreading (Fig. 11).

5.4. Implications for Mesozoic tectonic transition in the southern South China Sea

Mesozoic igneous rocks in the SCB are distributed mainly in four NE–SW-trending magmatic zones (Fig. 1a), namely, 254–215 Ma A-type granites and alkaline syenite plutons distributed along the Zhenghe–Dapu Fault, 200–177 Ma arc-related igneous rocks along the Dongsha–Talun–Yandang arc belt in the SCB continental margin, 185–169 Ma magmatic rocks along the Jiangshan–Shaoxing–Chenzhou–Linwu Fault (Qin–Hang belt), and 141–116 Ma A-type granites and bimodal magmatic rocks along the coastal area of the SCB. The development of these magmatic belts was associated with subduction of the Paleo-Pacific plate during the Mesozoic.

Triassic dacites (217 Ma) from Well NK-1 in the southern SCS and

Triassic A-type granites along the Zhenghe–Dapu Fault in the SCB are geochemically similar to A_2-type granites, indicating the presence of an extensional setting probably controlled by subduction of the Paleo-Pacific plate beneath the proto-Japan arc (Miao et al., 2021; Shen et al., 2018; Wang et al., 2005).

Arc-related granites with ages of 200–177 Ma along the NE–SW-trending Dongsha–Talun–Yandang magmatic arc belt formed in a continental arc of the Paleo-Pacific plate (Fig. 12a, b; Xu et al., 2017; Zhu et al., 2016). The 177 Ma CAB-like diorites from Well NK-1 might also have formed in a continental arc setting. In addition, Jurassic pelagic to terrigenous facies chert-clastic sequences in North Palawan (Faure and Ishida, 1990; Zamoras and Matsuoka, 2001) are comparable with cherts, siliceous clastic rocks, and pelagic limestones on Panay Island (Gabo et al., 2009; Zamoras et al., 2008), all of which are products of Early Jurassic oceanic plate subduction and consequent Jurassic subduction-related accretion (Xu et al., 2017; Zamoras and Matsuoka, 2001). Thus, a continental arc is inferred to have existed along the southern continental margin of the SCB during the Jurassic (Fig. 12a, b). Jurassic arc magmatism is further evidenced by coeval arc-related magmatic rocks in the Qin–Hang belt (185–170 Ma), which show enriched Sr—Nd isotopes with high $(^{87}Sr/^{86}Sr)_i$ ratios (0.7079–0.7192) and variable $\varepsilon_{Nd}(t)$ values (−7.0 to +2.3; Fig. 6a) and are interpreted to have formed by partial melting of Neoproterozoic arc-related material associated with the far-field effects of oblique subduction of the Paleo-Pacific plate (Xu et al., 2017). Furthermore, adakitic rocks (ca. 175 Ma) in the Qin–Hang belt are inferred to be products of remelting of a Neoproterozoic magmatic arc related to back-arc extension controlled by Paleo-Pacific plate subduction (Xia et al., 2016).

The presence of 144 Ma A-type granite at Haiyan in Guangdong province (Jia et al., 2018) is suggestive of an Early Cretaceous extensional setting in the coastal area of the SCB. The BABB-like diabases (124 ± 5 Ma) from Well NK-1, together with 139–116 Ma I-type and A-type granites in the coastal area of the SCB (Li et al., 2014), indicate the presence of a back-arc basin in the continental margin of the SCB. The diabase samples from Well NK-1, which formed during spreading of a back-arc basin, are geochemically similar to the Darvel Bay ophiolitic complexes in the north Borneo Block and Antique ophiolitic complexes on Panay Island, which have been regarded as remnants of PSCS oceanic crust (Omang and Barber, 1996; Tamayo et al., 2001; Yumul Jr et al., 2013; Figs. 4 and 10). Thus, the BABB-like diabase samples from Well NK-1 might be analogs of coeval oceanic crust of the PSCS. Early Cretaceous diabases in the Nansha Block, which intrude the preexisting continental margin, cannot be MORBs but might represent coeval BABB magmatism when the region changed from a back-arc basin setting into a nascent ocean. During the Cretaceous, southeastward spreading of the PSCS (Zahirovic et al., 2014) is consistent with NW-directed subduction of the Paleo-Pacific plate rather than northward subduction of the Neo-Tethys plate (Hall, 2012). Therefore, the PSCS is interpreted to have been a back-arc basin formed by retreat or rollback of the subducting Paleo-Pacific plate during the Early Cretaceous (Fig. 12c, d).

In summary, the two episodes of Mesozoic mafic magmatism inferred from rocks of Well NK-1 in the Nansha Block record the tectonic transition from continental arc to back-arc basin and even the nascent ocean of the PSCS in the southern continental margin of the SCB. This interpretation is consistent with the evolution of a subduction zone that changed regionally to an extensional setting owing to the retreat or rollback of the Paleo-Pacific plate.

6. Conclusions

(1) Diorites and diabases from Well NK-1 in the Nansha Block of the southern SCS were emplaced during the Early Jurassic (ca. 177 Ma) and Early Cretaceous (ca. 124 Ma), respectively.

(2) Diorite samples from Well NK-1 have geochemical affinities with CAB, and their mantle source was metasomatized by subducted
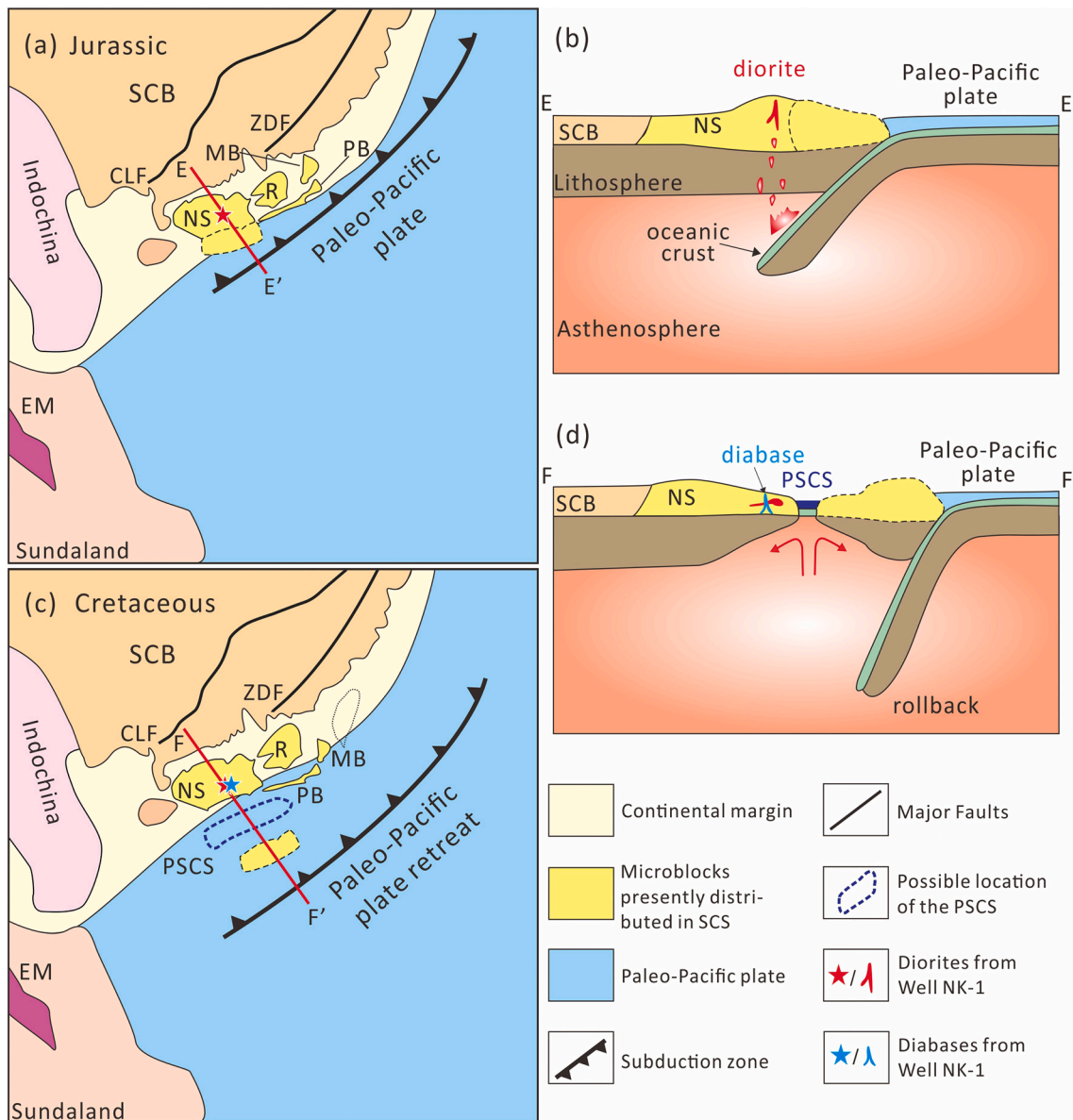
Fig. 12. Reconstructions of Southeast Asia from the Jurassic to Early Cretaceous. (a) During the Jurassic, the Nansha Block was attached to the SCB and the Paleo-Pacific plate subducted beneath the continental margin of the SCB; (b) schematic model of cross-section E–E' in (a); (c) during the Early Cretaceous, the PSCS was a back-arc basin that formed as a result of the retreat or roll-back of the subducting Paleo-Pacific plate; and (d) schematic model of cross-section F–F' in (c). Abbreviations: Eastern Malaysia (EM); Mindoro Block (MB); Nansha Block (NS); Palawan Block (PB); Reed Bank (R); Zhenghe–Dapu Fault (ZDF); and Chenzou–Linwu Fault (CLF).

sediment melts in a continental arc setting controlled by subduction of the Paleo-Pacific plate.

(3) Diabase samples from Well NK-1 are geochemically similar to BABB and were derived from partial melting of a mantle source that had been previously metasomatized by aqueous fluids from the subducting Paleo-Pacific slab.

(4) Early Cretaceous diabases in the Nansha Block might represent coeval magmatism corresponding to the development of a back-arc basin (and nascent ocean of the PSCS) associated with the retreat or rollback of the subducting Paleo-Pacific plate.

Supplementary data to this article can be found online at https://doi.org/10.1016/j.lithos.2021.106502.

Declaration of Competing Interest

The authors declare that they have no known competing financial interests or personal relationships that could have appeared to influence the work reported in this paper.

References

Baker, J., Peate, D., Waight, T., Meyzen, C., 2004. Pb isotopic analysis of standards and samples using a $^{207}Pb–^{204}Pb$ double spike and thallium to correct for mass bias with a double-focusing MC-ICP-MS. Chem. Geol. 211, 275–303. https://doi.org/10.1016/j.chemgeo.2004.06.030.

Briais, A., Patriat, P., Tapponnier, P., 1993. Updated interpretation of magnetic anomalies and seafloor spreading stages in the South China Sea, implications for the Tertiary tectonics of Southeast Asia. J. Geophys. Res. Solid Earth 98 (B4), 6299–6328. https://doi.org/10.1029/92JB02280.

Chauvel, C., Blichert-Toft, J., 2001. A hafnium isotope and trace element perspective on melting of the depleted mantle. Earth Planet. Sci. Lett. 190 (3–4), 137–151. https://doi.org/10.1016/S0012-821X(01)00379-X.

Chauvel, C., Lewin, E., Carpentier, M., Arndt, N.T., Marini, J.C., 2008. Role of recycled oceanic basalt and sediment in generating the Hf–Nd mantle array. Nat. Geosci. 1 (1), 64–67. https://doi.org/10.1038/ngeo.2007.51.

Cullen, A.B., 2010. Transverse segmentation of the Baram-Balabac Basin, NW Borneo: refining the model of Borneo's tectonic evolution. Pet. Geosci. 16, 3–29. https://doi.org/10.1144/1354-079309-828.

Faure, M., Ishida, K., 1990. The Mid-Upper Jurassic olistostrome of the west Philippines: a distinctive key-marker for the North Palawan block. J. SE Asian Earth Sci. 4, 61–67. https://doi.org/10.1016/0743-9547(90)90026-A.

Floyd, P.A., Shail, R., Leveridge, B.E., Franke, W., 1991. Geochemistry and provenance of Rhenohercynian synorogenic sandstones: implications for tectonic environment discrimination. Geol. Soc. London Spec. Publ. 57 (1), 173–188. https://doi.org/10.1144/gsl.sp.1991.057.01.14.

Gabo, J.A.S., Dimalanta, C.B., Asio, M.G.S., Queaño, K.L., Yumul Jr., G.P., Imai, A., 2009. Geology and geochemistry of the clastic sequences from Norwestern Panay (Philippines): implications for provenance and geotectonic setting. Tectonophysics 479, 111–119. https://doi.org/10.1016/j.tecto.2009.02.004.

Gao, P., Zheng, Y.F., Zhao, Z.F., 2017. Triassic granites in South China: a geochemical perspective on their characteristics, petrogenesis, and tectonic significance. Earth Sci. Rev. 173, 266–294. https://doi.org/10.1016/j.earscirev.2017.07.016.

Gao, J., Yu, Y., Song, W., Gao, S.S., Liu, K.H., 2020. Crustal modifications beneath the central Sunda plate associated with the Indo-Australian subduction and the evolution of the South China Sea. Phys. Earth Planet. Inter. 306, 106539. https://doi.org/10.1016/j.pepi.2020.106539.

Gibaga, C.R.L., Arcilla, C.A., HoanG, N., 2020. Volcanic rocks from the Central and Southern Palawan Ophiolites, Philippines: tectonic and mantle heterogeneity constraints. J. Asian Earth Sci. 4, 100038. https://doi.org/10.1016/j.jaesx.2020.100038.

Gribble, R.F., Stern, R.J., Bloomer, S.H., Stüben, D., O'Hearn, T., Newman, S., 1996. MORB mantle and subduction components interact to generate basalts in the southern Mariana Trough back-arc basin. Geochim. Cosmochim. Acta 60 (12), 2153–2166. https://doi.org/10.1016/0016-7037(96)00078-6.

Gribble, R.F., Stern, R.J., Newman, S., Bloomer, S.H., O'Hearn, T., 1998. Chemical and isotopic composition of lavas from the northern Mariana Trough: implications for magmagenesis in back-arc basins. J. Petrol. 39 (1), 125–154. https://doi.org/10.1093/petroj/39.1.125.

Hall, R., 2012. Late Jurassic–Cenozoic reconstructions of the Indonesian region and the Indian Ocean. Tectonophysics 570–571 (11), 1–41. https://doi.org/10.1016/j.tecto.2012.04.021.

Hall, R., van Hattum, M.W., Spakman, W., 2008. Impact of India–Asia collision on SE Asia: the record in Borneo. Tectonophysics 451 (1–4), 366–389. https://doi.org/10.1016/j.tecto.2007.11.058.

Handley, H.K., Macpherson, C.G., Davidson, J.P., Berlo, K., Lowry, D., 2007. Constraining fluid and sediment contributions to subduction-related magmatism in Indonesia: Ijen Volcanic Complex, Indonesia. J. Petrol. 48, 1155–1183. https://doi.org/10.1093/petrology/egm013.

Hart, S.R., 1984. A large-scale isotope anomaly in the southern hemisphere mantle. Nature 309, 753–757. https://doi.org/10.1038/309753a0.

Hickey-Vargas, R., Bizimis, M., Deschamps, A., 2008. Onset of the Indian Ocean isotopic signature in the Philippine Sea Plate: Hf and Pb isotope evidence from Early Cretaceous terranes. Earth Planet. Sci. Lett. 268 (3–4), 255–267. https://doi.org/10.1016/j.epsl.2008.01.003.

Hirahara, Y., Kimura, J.I., Senda, R., Miyazaki, T., Kawabata, H., Takahashi, T., Chang, Q., Vaglarov, B.S., Sato, T., Kodaira, S., 2015. Geochemical variations in Japan Sea back-arc basin basalts formed by high-temperature adiabatic melting of mantle metasomatized by sediment subduction components. Geochem. Geophys. Geosyst. 16, 1324–1347. https://doi.org/10.1002/2015GC005720.

Hoang, N., Uto, K., 2006. Upper mantle isotopic components beneath the Ryukyu Arc system: evidence for 'back-arc' entrapment of Pacific MORB mantle. Earth Planet. Sci. Lett. 249, 229–240. https://doi.org/10.1016/j.epsl.2006.07.021.

Iwamori, H., Nakamura, H., 2015. Isotopic heterogeneity of oceanic, arc and continental basalts and its implications for mantle dynamics. Gondwana Res. 27, 1131–1152. https://doi.org/10.1016/j.gr.2014.09.003.

Jia, X.H., Xie, G.G., Meng, D.L., Wan, L., Wu, J., Bu, J.J., Wu, F.Q., Zeng, H.L., Lu, J.W., Zhan, R.H., 2018. Petrogenesis and implications of the Haiyan A-type granites and mafic microgranule enclaves in Southern Guangdong Province. Earth Sci. 43 (7), 2294–2312 (in Chinese with English abstract).

Koppers, A.A., 2002. Ar–Ar CALC-software for $^{40}Ar/^{39}Ar$ age calculations. Comput. Geosci. 28 (5), 605–619. https://doi.org/10.1016/S0098-3004(01)00095-4.

Kudrass, H.R., Wiedicke, M., Cepek, P., Muller, P., 1986. Mesozoic and Cainozoic rocks dredged from the South China Sea (Reed Bank area) and Sulu Sea and their significance for plate–tectonic reconstructions. Mar. Pet. Geol. 3 (1), 19–30. https://doi.org/10.1016/0264-8172(86)90053-X.

Larsen, H.C., Mohn, G., Nirrengarten, M., Sun, Z., Stock, J., Jian, Z., Klaus, A., AlvarezZarikian, C.A., Boaga, J., Bowden, S.A., Briais, A., Chen, Y., Cukur, D., Dadd, K., Ding, W., Dorais, M., Ferré, E.C., Ferreira, F., Furusawa, A., Gewecke, A., Hinojosa, J., Höfig, T.W., Hsiung, K.H., Huang, B., Huang, E., Huang, X.L., Jiang, S., Jin, H., Johnson, B.G., Kurzawski, R.M., Lei, C., Li, B., Li, L., Li, Y., Lin, J., Liu, C., Liu, C., Liu, Z., Luna, A.J., Lupi, C., McCarthy, A., Ningthoujam, L., Osono, N., Peate, D.W., Persaud, P., Qiu, N., Robinson, C., Satolli, S., Sauermilch, I., Schindlbeck, J.C., Skinner, S., Straub, S., Su, X., Su, C., Tian, L., van der Zwan, F.M., Wan, S., Wu, H., Xiang, R., Yadav, R., Yi, L., Yu, P.S., Zhang, C., Zhang, J., Zhang, Y., Zhao, N., Zhong, G., Zhong, L., 2018. Rapid transition from continental breakup to igneous oceanic crust in the South China Sea. Nat. Geosci. 11, 782–789. https://doi.org/10.1038/s41561-018-0198-1.

Le Maitre, R.W., 1989. A Classification of Igneous Rocks and Glossary of Terms, Recommendation of the IOU Subcommission on the Systematics of Igneous Rocks. Blackwell, Oxford.

Li, X.H., Liu, D.Y., Sun, M., 2004. Precise Sm–Nd and U–Pb isotopic dating of the super-giant Shizhuyuan polymetallic deposit and its host granite, Southeast China. Geol. Mag. 141, 225–231. https://doi.org/10.1017/S0016756803008823.

Li, X.H., Li, Z.X., Wingate, M.T.D., 2006. Geochemistry of the 755 Ma Mundine Well dyke swarm, northwestern Australia, part of a Neoproterozoic mantle superplume beneath Rodinia. Precambrian Res. 146, 1–15. https://doi.org/10.1016/j.precamres.2005.12.007.

Li, Z., Qiu, J.S., Yang, X.M., 2014. A review of the geochronology and geochemistry of Late Yanshanian (Cretaceous) plutons along the Fujian coastal area of southeastern China: Implications for magma evolution related to slab break-off and rollback in the Cretaceous. Earth Sci. Rev. 128, 232–248. https://doi.org/10.1016/j.earscirev.2013.09.007.

Litvak, V.D., Poma, S., 2010. Geochemistry of mafic Paleocene volcanic rocks in the Valle del Cura region: Implications for the petrogenesis of primary mantle– derived melts over the Pampean flat–slab. J. S. Am. Earth Sci. 29, 705–716. https://doi.org/10.1016/j.jsames.2010.01.001.

McArthur, J.M., 1994. Recent trends in strontium isotope stratigraphy. Terra Nova 6 (4), 331–358. https://doi.org/10.1111/j.1365-3121.1994.tb00507.x.

Miao, X.Q., Huang, X.L., Yan, W., Yang, F., Zhang, W.F., Cai, Y.X., Yu, Y., He, P.L., 2021. Late triassic dacites from well NK-1 in the nansha block: constraints on the mesozoic tectonic evolution of the Southern South China sea margin. Lithos 398–399, 106337. https://doi.org/10.1016/j.lithos.2021.106337.

Morley, C.K., 2012. Late Cretaceous-Early Palaeogene tectonic development of SE Asia. Earth Sci. Rev. 115 (S1–2), 37–75. https://doi.org/10.1016/j.earscirev.2012.08.002.

Omang, S.A.K., Barber, A.J., 1996. Origin and tectonic significance of the metamorphic rocks associated with the Darvel Bay Ophiolite, Sabah, Malaysia. Geol. Soc. London Spec. Publ. 106 (1), 263–279. https://doi.org/10.1144/GSL.SP.1996.106.01.17.

Patino, L.C., Velbel, M.A., Price, J.R., Wade, J.A., 2004. Trace element mobility during spheroidal weathering of basalts and andesites in Hawaii and Guatemala. Chem. Geol. 202, 343–364. https://doi.org/10.1016/j.chemgeo.2003.01.002.

Pearce, J.A., Stern, R.J., Bloomer, S.H., Fryer, P., 2005. Geochemical mapping of the Mariana arc-basin system: Implications for the nature and distribution of subduction components. Geochem. Geophys. Geosyst. 6, Q07006 https://doi.org/10.1029/2004GC000895.

Plank, T., Langmuir, C.H., 1998. The chemical composition of subducting sediment and its consequences for the crust and mantle. Chem. Geol. 145, 325–394. https://doi.org/10.1016/S0009-2541(97)00150-2.

Polat, A., Hofmann, A.W., 2003. Alteration and geochemical patterns in the 3.7–3.8 Ga Isua greenstone belt, West Greenland. Precambrian Res. 126, 197–218. https://doi.org/10.1016/S0301-9268(03)00095-0.

Regelous, M., Collerson, K.D., Ewart, A., Wendt, J.I., 1997. Trace element transport rates in subduction zones: evidence from Th, Sr and Pb isotope data for Tonga-Kermadec arc lavas. Earth Planet. Sci. Lett. 150 (3–4), 291–302. https://doi.org/10.1016/S0012-821X (97)00107-6.

Rudnick, R., Gao, S., 2003. Composition of the continental crust. Treatise Geochem. 3, 1–64. https://doi.org/10.1016/B978-0-08-095975-7.00301-6.

Schmidt, M.W., Jagoutz, O., 2017. The global systematics of primitive arc melts. Geochem. Geophys. Geosyst. 18, 2817–2854. https://doi.org/10.1002/2016GC006699.

Shao, L., Cao, L., Qiao, P., Zhang, X., Li, Q., Van Hinsbergen, D.J.J., 2017. Cretaceous-Eocene provenance connections between the Palawan Continental Terrane and the northern South China Sea margin. Earth Planet. Sci. Lett. 477, 97–107. https://doi.org/10.1016/j.epsl.2017.08.019.

Shen, L.W., Yu, J.H., O'Reilly, S.Y., Griffin, W.L., Zhou, X.Y., 2018. Subduction-related middle Permian to Early Triassic magmatism in central Hainan Island, South China. Lithos 318–319, 158–175. https://doi.org/10.1016/j.lithos.2018.08.009.

Shinjo, R., Chung, S.L., Kato, Y., Kimura, M., 1999. Geochemical and Sr–Nd isotopic characteristics of volcanic rocks from the Okinawa Trough and Ryukyu Arc: implications for the evolution of a young, intracontinental back-arc basin. J. Geophys. Res. 104 (B5), 10591–10608. https://doi.org/10.1029/1999JB900040.

Shuto, K., Ishimoto, H., Hirahara, Y., Sato, M., Matsui, K., 2006. Geochemical secular variation of magma source during Early to Middle Miocene time in the Niigata area, NE Japan: Asthenospheric mantle upwelling during back-arc basin opening. Lithos 83, 1–33. https://doi.org/10.1016/j.lithos.2005.06.001.

Steiger, R.H., Jäger, E., 1977. Subcommission on Geochronology: convention on the use of decay constants in geo- and cosmochronology. Earth Planet. Sci. Lett. 36, 359–362. https://doi.org/10.1016/0012-821X(77)90060-7.

Stern, R.J., Lin, P.N., Morris, J.D., Jackson, M.C., Fryer, P., Bloomer, S.H., Ito, E., 1990. Enriched back-arc basin basalts from the northern Mariana Trough: implications for the magmatic evolution of back-arc basins. Earth Planet. Sci. Lett. 100 (1), 210–225. https://doi.org/10.1016/0012-821X(90)90186-2.

Suggate, S.M., Cottam, M.A., Hall, R., Sevastjanova, I., Forster, M.A., White, L.T., Armstrong, R.A., Carter, Andrew, Mojares, E., 2014. South China continental margin signature for sandstones and granites from Palawan, Philippines. Gondwana Res. 26, 699–718. https://doi.org/10.1016/j.gr.2013.07.006.

Sun, W.D., 2016. Initiation and evolution of the South China Sea: an overview. Acta Geochim. 35 (3), 226. https://doi.org/10.1007/s11631-016-0113-7.

Sun, S.S., McDonough, W.F., 1989. Chemical and isotopic systematics of oceanic basalts, implications for mantle composition and processes. Geol. Soc. London Spec. Publ. 42, 313–345. https://doi.org/10.1144/GSL.SP.1989.042.01.19.

Tamayo, R.A., Yumul, J.R.G.P., Maury, R.C., Polvé, M., Cotten, J., Bohn, M., 2001. Petrochemical investigation of the Antique Ophiolite (Philippines): implications on volcanogenic massive sulfide and podiform chromitite deposits. Resour. Geol. 51 (2), 145–164. https://doi.org/10.1111/j.1751-3928.2001.tb00088.x.

Tannaka, T., Togashi, S., Kamioka, H., Amakawa, H., Kagami, H., Hamamoto, T., Yuhara, M., Orihashi, Y., Yoneda, S., Shimizu, H., Kunimaru, T., Takahashi, K., Yanagi, T., Nakano, T., Fujimaki, H., Shinjo, R., Asahara, Y., Tanimizu, M., Dragusanu, C., 2000. JNdi-1, a neodymium isotopic reference in consistency with LaJolla neodymium. Chem. Geol. 168, 279–281. https://doi.org/10.1016/S0009-2541(00)00198-4.

Tapponnier, P., Peltzer, G., Ledain, A.Y., Armijo, R., Cobbold, P., 1982. Propagating extrusion tectonics in Asia: new insights from simple experiments with plasticine. Geology 10 (12), 611–616. https://doi.org/10.1130/0091-7613(1982)10<611:PETIAN>2.0.CO;2.

Taylor, B., Hayes, D.E., 1982. Origin and history of the South China Sea Basin. In: Hayes, D.E. (Ed.), The Tectonic and Geologic Evolution of Southeast Asian Seas and Islands, Part 2, American Geophysical Union Geophysical Monograph, Washington, DC, vol. 27, pp. 23–56.

Todd, E., Gill, J.B., Wysoczanski, R.J., Handler, M.R., Wright, I.C., Gamble, J.A., 2010. Sources of constructional cross-chain volcanism in the southern Havre Trough: New insights from HFSE and REE concentration and isotope systematics. Geochem. Geophys. Geosyst. 11, Q04009 https://doi.org/10.1029/2009 GC002888.

Tollstrup, D.L., Gill, J.B., 2005. Hafnium systematics of the Mariana arc: evidence for sediment melt and residual phases. Geology 33, 737–740. https://doi.org/10.1130/G21639.1.

Viruete, J.E., Joubert, M., Urien, P., Friedman, R., Weis, D., Ullrich, T., Pérez-Estaún, A., 2008. Caribbean island-arc rifting and back-arc basin development in the late cretaceous: geochemical, isotopic and geochronological evidence from Central Hispaniola. Lithos 104 (1–4), 378–404. https://doi.org/10.1016/j.lithos.2008.01.003.

Wang, Q., Li, J.W., Jian, P., Zhao, Z.H., Xiong, X.L., Bao, Z.W., Xu, J.F., Li, C.F., Ma, J.L., 2005. Alkaline syenites in eastern Cathaysia (South China), link to Permian-Triassic transtension. Earth Planet. Sci. Lett. 230 (3–4), 339–354. https://doi.org/10.1016/j.epsl.2004.11.023.

Wang, Q., Wyman, D.A., Xu, J.F., Dong, Y., Vasconcelos, P.M., Pearson, N., Wan, Y., Dong, H., Li, C., Yu, Y., 2008. Eocene melting of subducting continental crust and early uplifting of Central Tibet: evidence from central-western Qiangtang high-K calc-alkaline andesites, dacites and rhyolites. Earth Planet. Sci. Lett. 272 (1), 158–171. https://doi.org/10.1016/j.epsl.2008.04.034.

Wei, G.J., Liang, X.R., Li, X.H., Liu, Y., 2002. Precise measurement of Sr isotopic compositions of liquid and solid base using (LA) MCICP-MS. Geochimica 31, 295–305 (in Chinese with English abstract).

Woodhead, J.D., Hergt, J.M., 2005. Preliminary appraisal of seven natural zircon reference materials for in situ Hf isotope determination. Geostand. Geoanal. Res. 29, 183–195. https://doi.org/10.1111/j.1751-908X.2005.tb00891.x.

Woodhead, J.D., Hergt, J.M., Davidson, J.P., Eggins, S.M., 2001. Hafnium isotope evidence for 'conservative' element mobility during subduction processes. Earth Planet. Sci. Lett. 192, 331–346. https://doi.org/10.1016/S0012-821X(01)00453-8.

Workman, R.K., Hart, S.R., 2005. Major and trace element composition of the depleted MORB mantle (DMM). Earth Planet. Sci. Lett. 231, 53–72. https://doi.org/10.1016/j.epsl.2004.12.005.

Wu, Jonny, Suppe, J., 2018. Proto–South China Sea Plate tectonics using subducted slab constraints from tomography. J. Earth Sci. 29 (6), 1304–1318. https://doi.org/10.1007/s12583-017-0813-x.

Xia, Y., Xu, X.S., Liu, L., 2016. Transition from adakitic to bimodal magmatism induced by the Paleo-Pacific plate subduction and slab rollback beneath SE China: evidence from petrogenesis and tectonic setting of the dike swarms. Lithos 244, 182–204. https://doi.org/10.1016/j.lithos.2015.12.006.

Xu, C.H., Zhang, L., Shi, H.S., Brix, M.R., Huhma, H., Chen, L., Zhang, M., Zhou, Z., 2017. Tracing an early Jurassic magmatic arc from South to East China Seas. Tectonics 36, 466–492. https://doi.org/10.1002/2016TC004446.

Xu, W.C., Luo, B.J., Xu, Y.J., Wang, L., Chen, Q., 2018. Geochronology, geochemistry, and petrogenesis of Late Permian to Early Triassic mafic rocks from Darongshan, South China, Implications for ultrahigh-temperature metamorphism and S-type granite generation. Lithos 308–309, 168–180. https://doi.org/10.1016/j.lithos.2018.03.004.

Yan, Q.S., Shi, X.F., 2014. Petrologic perspectives on tectonic evolution of a nascent basin (Okinawa Trough) behind Ryukyu Arc: a review. Acta Oceanol. Sin. 33 (4), 1–12. https://doi.org/10.1007/s13131-014-0400-2.

Yan, Q.S., Shi, X.F., Liu, J.H., Wang, K.S., Bu, W.R., 2010. Petrology and geochemistry of mesozoic granitic rocks from the nansha micro-block, the South China Sea: constraints on the basement nature. J. Asian Earth Sci. 37 (2), 130–139. https://doi.org/10.1016/j.jseaes.2009.08.001.

Yu, M.M., Dilek, Y., Yumul Jr., G.P., Dimalanta, C.B., 2020. Slab-controlled elemental–isotopic enrichments during subduction initiation magmatism and variations in forearc chemostratigraphy. Earth Planet. Sci. Lett. 538, 116217. https://doi.org/10.1016/j.epsl.2020.116217.

Yumul Jr., G.P., Dimalanta, C.B., Tamayo Jr., R.A., Faustino-Eslava, D.V., 2013. Geological features of a collision zone marker: the Antique ophiolite complex (western Panay, Philippines). J. Asian Earth Sci. 65, 53–63. https://doi.org/10.1016/j.jseaes.2012.08.017.

Zahirovic, S., Seton, M., Müller, R.D., 2014. The Cretaceous and Cenozoic tectonic evolution of Southeast Asia. Sol. Earth 2014 (5), 227–273. https://doi.org/10.5194/se-5-227-2014.

Zamoras, L.R., Matsuoka, A., 2001. Malampaya sound group: a Jurassic–Early Cretaceous accretionary complex in Busuanga Island, North Palawan Block (Philippines). J. Geol. Soc. Jpn. 107, 316–336. https://doi.org/10.5575/geosoc.107.316.

Zamoras, L.R., Montes, M.G.A., Queaño, K.L., Marquez, E.J., Dimalanta, C.B., Gabo, J.A.S., Yumul Jr., G.P., 2008. The Buruanga Peninsula and the Antique range: two contrasting terranes in Northwest Panay, Philippines featuring an arc-continent collision zone. Island Arc 17, 443–457. https://doi.org/10.1111/j.1440-1738.2008.00645.x.

Zhu, K.Y., Li, Z.X., Xu, X.S., Wilde, S.A., Chen, H.L., 2016. Early Mesozoic ferroan (A-type) and magnesian granitoids in eastern South China: tracing the influence of flat-slab subduction at the western Pacific margin. Lithos 240–243 (10), 371–381. https://doi.org/10.1016/j.lithos.2015.11.025.